



HAL
open science

Seismo-tectonic model for the southern Pre-Rif border (Northern Morocco): Insights from morphochronology

Kamal Agharroud, Lionel Siame, Abdelkhalak Ben Moussa, Olivier Bellier, Valéry Guillou, Jules Fleury, Younes El Kharim

► To cite this version:

Kamal Agharroud, Lionel Siame, Abdelkhalak Ben Moussa, Olivier Bellier, Valéry Guillou, et al.. Seismo-tectonic model for the southern Pre-Rif border (Northern Morocco): Insights from morphochronology. *Tectonics*, 2021, 10.1029/2020TC006633 . hal-03194765

HAL Id: hal-03194765

<https://hal.science/hal-03194765>

Submitted on 9 Apr 2021

HAL is a multi-disciplinary open access archive for the deposit and dissemination of scientific research documents, whether they are published or not. The documents may come from teaching and research institutions in France or abroad, or from public or private research centers.

L'archive ouverte pluridisciplinaire **HAL**, est destinée au dépôt et à la diffusion de documents scientifiques de niveau recherche, publiés ou non, émanant des établissements d'enseignement et de recherche français ou étrangers, des laboratoires publics ou privés.

1 **Seismo-tectonic model for the southern Pre-Rif border (Northern Morocco): Insights**
2 **from morphochronology**

3 **Kamal Agharroud¹, Lionel L. Siame^{*,2}, Abdelkhalak Ben Moussa¹, Olivier Bellier², Valéry**
4 **Guillou², Jules Fleury², Younes El Kharim¹**

5 ¹Faculté des Sciences de l'Université Abdelmalek Essaâdi, Département de Géologie, Tétouan,
6 Maroc.

7 ²Aix Marseille Univ., CNRS, IRD, INRAE, Coll France, CEREGE, Aix-en-Provence, France.

8 *Corresponding author: Lionel Siame (siame@cerege.fr)

9
10 **Key Points:**

- 11 • High resolution digital topography helps locate morphological indexes of active tectonics
12 in Morocco.
- 13 • Cosmogenic nuclides allow placing time constraints for landscape development in the
14 Southern Rif Front.
- 15 • The Southern Rif Front is an important geodynamic boundary with a non-negligible
16 seismogenic potential.

17 (The above elements should be on a title page)

18

19 Abstract

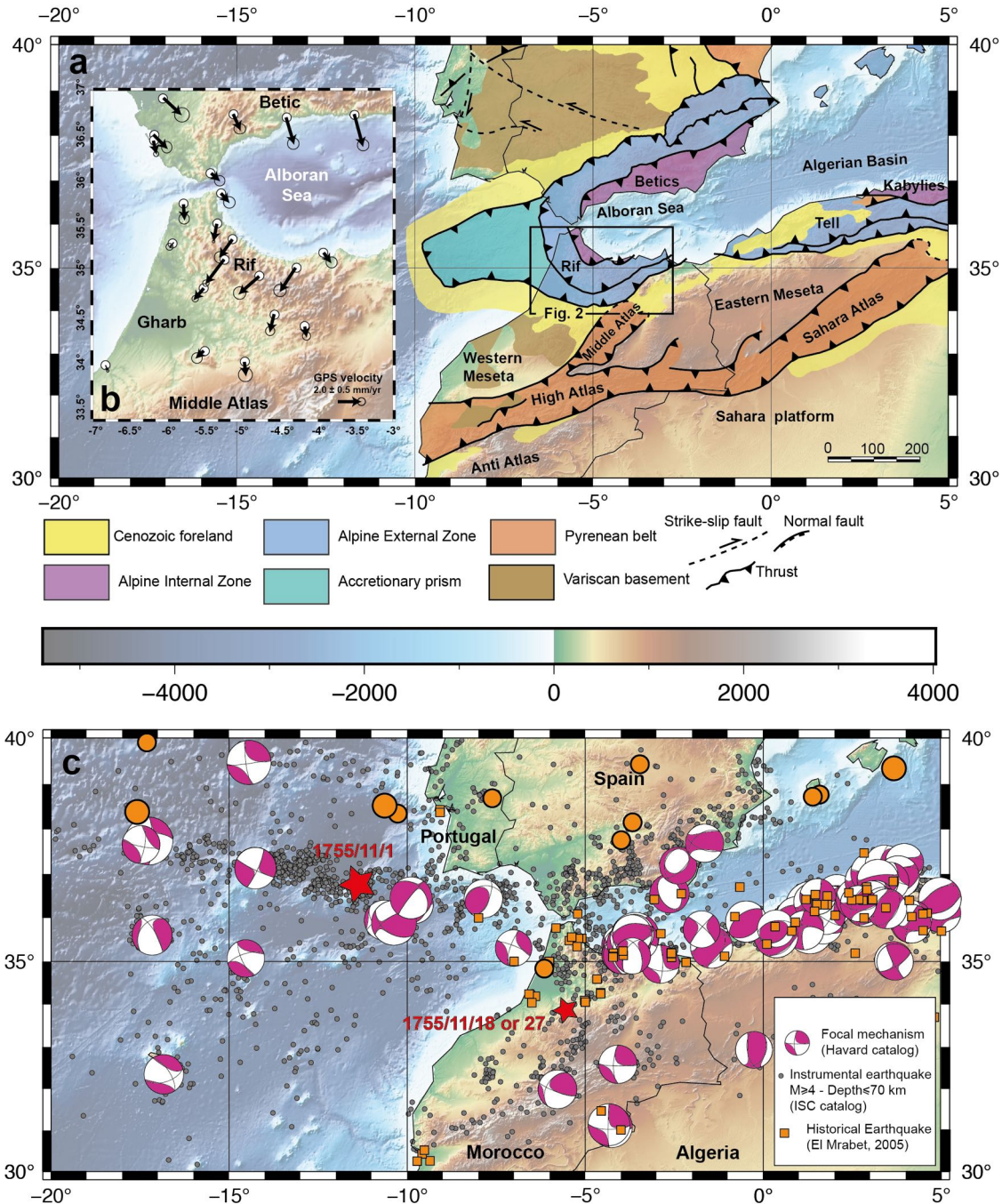
20 Located at the southern boundary of the Alpine chain in Morocco, the deformation front of the
21 Southern Rif Mountains is a region of moderate tectonic activity, which makes it a good natural
22 laboratory to understand whether, and how, low compressional strains are located on specific
23 structures. Along the ≈ 80 km-long left-lateral, transpressive and reverse fault zone that runs at the
24 toe of the Pre-Rif Ridges, an analysis of high-resolution digital topography provides new
25 geomorphic lines of evidence supporting Quaternary activity along, 20 km-long fault segments.
26 The fault zone can be divided into the Meknès and the Fès segments, which are constrained at
27 depth by reactivated, NE-trending basement faults, delimitating paleo-grabens associated with the
28 Late Triassic-Jurassic opening of the Atlantic Ocean. For selected sites, we used *in situ*-produced
29 ^{36}Cl , ^{10}Be and ^{26}Al and high-resolution topography to infer the timing of abandonment of fluvial
30 markers, which suggest incision rates on the order of 0.6-2 mm/yr. Given their lengths, scaling
31 laws suggest that the identified fault segments should root at about 7-12 km-depth, possibly
32 reactivating former basement normal faults and making them potential seismogenic sources
33 capable of generating Mw6+ earthquakes, with return times of the order of several hundreds of
34 years. Our new morphochronological dataset confirms that the Southern Rif deformation front is
35 a key structure that may have accommodated most of the lateral extrusion of the Rif between the
36 Nubia and Iberia tectonic plates.

37 1 Introduction

38 In intraplate tectonic regions characterized by moderate seismic activity, the recognition of active
39 zones of deformation has long been a challenging task (*e.g.*, Landgraf et al., 2017). Like Northern
40 Africa, such regions are generally characterized by low hazard but high risk due to the
41 concentrations highly vulnerable population and/or infrastructures (Moreno et al., 2004).
42 Moreover, when low strain rates are combined with meteorological and anthropogenic overprints,
43 the geomorphic signatures associated with active faults fade away as fault slip rates decrease.
44 Consequently, diagnostic criteria established in areas of high strain rates may not be effectively
45 applied. Furthermore, low-levels of seismic strain induce low displacement rates, which may be
46 distributed over numerous fault segments rather than localized on a single fault. At the regional
47 scale, such a distribution of the tectonic deformation can also obscure the seismogenic potential of
48 any given single structure, as, for example, the La Rouvière Fault reactivation during the 2019

49 Mw 4.9 Le Teil Earthquake (Ritz et al., 2020), in southeastern France, which was previously
50 considered as inactive (Jomard et al., 2017).

51 Part of the peri-Mediterranean Alpine chain surrounding the Alboran Sea, the Rif Mountain belt
52 in Morocco is an area of moderate tectonic activity. Located within the diffuse convergence zone
53 between the Nubia and Iberia plates (Fig. 1), this region experienced an oblique NW-SE
54 shortening, with an estimated rate of about 4 mm/yr from global positioning system (GPS) data
55 (McClusky et al., 2003) and geologically current plate motions (DeMets et al., 2010). At a first
56 order, the present-day pattern of GPS displacement is in good agreement with the regional
57 evidence for tectonic activity in Northern Morocco (Morel and Meghraoui, 1996) and in the Baetic
58 Ranges (Giaconia et al., 2012), which indicates a combination of crustal shortening in the Rif and
59 extension in the Alboran Sea (*e.g.*, Vernant et al., 2010). However, the southward-directed crustal
60 motions observed in the Central Rif (Fig. 1), almost normal to the direction of Nubia-Iberia plate
61 motion, are incompatible with a simple two-plate model (Fadil et al., 2006; Vernant et al., 2010;
62 Pérouse et al., 2010). This particular situation is still a matter of debate and models involving
63 complex relationship between mantle processes and crustal tectonics have been put forward such
64 as, among others, oceanic lithosphere slab rollback or slab break-off of a subducting continental
65 lithosphere (*e.g.*, Bazada et al., 2013 and references therein). Recent numerical models and gravity
66 data indeed suggest an efficient coupling between the upper mantle and the crust (*e.g.*, Baratin et
67 al., 2016), which could be triggered by a rollback of the delaminated African lithospheric mantle
68 pulled by a sinking oceanic Western Mediterranean slab (*e.g.*, Faccenna et al., 2004; Bezada et al.,
69 2013). These recent advances in geodesy, seismology, and gravimetry indicate that much of the
70 Rif kinematics cannot be simply associated with the convergence between the Nubia and Iberia
71 plates, but is rather linked to some ongoing delamination and convective removal of the
72 lithospheric mantle beneath the orogen and back-arc opening in the Alboran Sea (Vernant et al.,
73 2010). This complex geodynamic setting yielded shortening in the upper brittle crust
74 approximately along the southern termination of the Rif, as defined by GPS measurements and
75 fault block models (Fadil et al., 2006; Vernant et al., 2010; Koulali et al., 2011).



76

77 **Figure 1.** Geodynamic setting of Morocco. (a) Simplified map of the major Cenozoic structural trends
 78 centered on the Baetic-Rif Belt (modified after Etheve et al., 2016); (b) GPS-derived kinematics (relative
 79 to fixed Nubia) in northern Morocco and in the Alboran region (after Kouali et al., 2011); (c) Map of the
 80 instrumental (International Seismological Center, 2020), focal mechanisms (Harvard global centroid
 81 moment tensor catalogue; e.g., Dziewonski et al., 1981; Ekström & Dziewonski, 2012), and historical
 82 epicentres in the Maghreb region (El Mrabet, 2005). Red stars locate the epicentre areas of the November
 83 1, 1755 and November 18 or 27, 1755 (see text for discussion).

84 While geomorphic studies have long demonstrated the tectonic activity of the Rif and the Pre-Rif
85 Ridges (Morel, 1988, 1989), it is only recently that dating techniques such as optically-stimulated
86 luminescence or *in situ*-produced cosmogenic nuclides have enabled determination of time
87 constraints on fault activity in the Rif, such as along the Nekor Fault (Poujol et al., 2014) or the
88 Pre-Rif Ridges (Poujol et al., 2017). The latter have also been identified as a probable source for
89 several historical earthquakes in the Fès-Meknès region (Moratti et al., 2003; El Mrabet, 2005;
90 Chalouan et al., 2014; Poujol et al., 2017) but a reappraisal of the morpho-structures associated
91 with the Pre-Rif front, and their relationships with inherited basement structures, is still needed in
92 order to better characterize their segmentation, kinematics, and seismogenic potential.

93 This study presents a new set of diagnostic criteria to identify and characterize the tectonic activity
94 of the faults running along the southern Pre-Rif border, taking into account different spatial scales
95 and time windows (Fig. 2). Starting from a regional reappraisal of already published data, we
96 provide a new morpho-chronological dataset, using structural morphology and cosmogenic
97 exposure dating (*in situ* produced ^{10}Be , ^{26}Al and ^{36}Cl) of alluvial terraces, bringing additional lines
98 of evidence for tectonic activity along the boundary between the Pre-Rif Ridges and the Saïss
99 Basin (Fig. 2). All together, this new data set enables us to identify and characterize active
100 structures with slip rates of the order of about 1 mm/yr, providing a basis for a renewed seismic
101 hazard assessment in a region where the large cities of Meknès and Fès host nearly 2 million
102 people.

103 **2 Active tectonics of Northern Morocco**

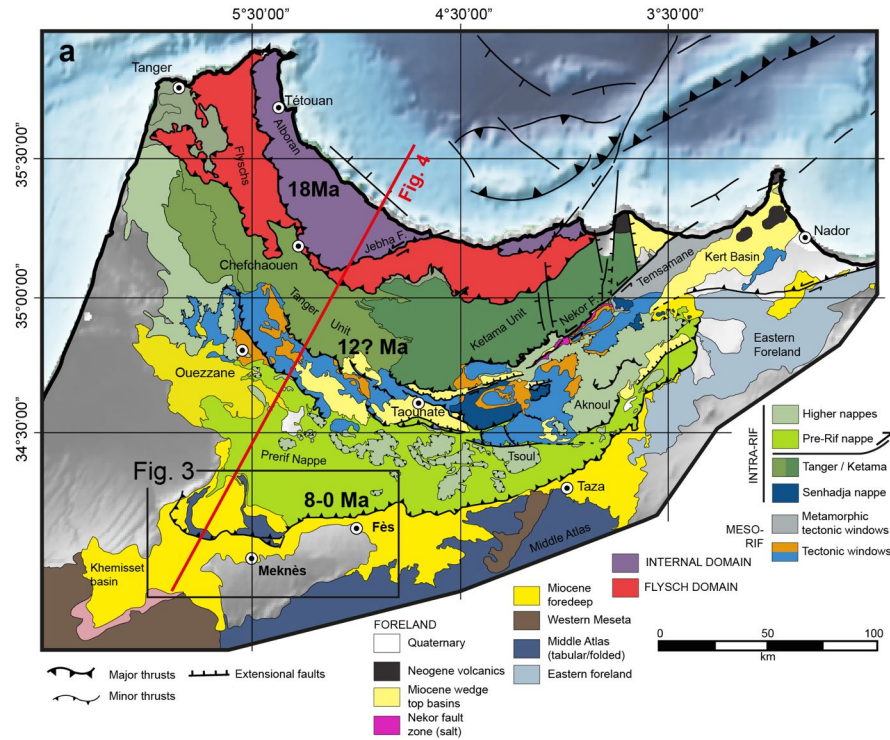
104 Although the seismic hazard in Morocco is not as important as in other Mediterranean countries
105 like Italy, Turkey or Greece, it is far from being negligible. Indeed, the relatively superficial nature
106 of the seismicity may combine with weak ground mechanical properties to induce relatively strong
107 accelerations that may lead to significant damage to buildings that do not always meet construction
108 standards (Mourabit et al., 2014). During the last decades, Morocco suffered from several
109 destructive earthquakes such as the Mw 5.9 Agadir event in 1960 or more recently those that struck
110 the region of Al Hoceima in 1994 (Mw 5.7), 2004 (Mw 6.3) and 2016 (Mw 6.3).

111 In the Gulf of Cadiz, oceanic earthquakes may also be tsunamigenic, like the *Lisbon Earthquake*
112 on November 1st, 1755 ($M \approx 8.5-9$) (Martinez-Solares et al., 1979; Johnston, 1996; Gutscher, 2004;
113 Gutscher et al., 2006). However, the frequency of such large events remains a major unknown

114 given the uncertainties weighting on the length of the seismic cycle in a context where the tectonic
115 rates are only a few mm/yr (Vernant et al., 2010). In the Gulf of Cadiz, the strongest recent
116 earthquake is that of February 28, 1969 (Mw 7.8; Fukao, 1973). Since 1970, only 19 events have
117 been recorded with a magnitude larger than five and only two with a magnitude larger than six
118 (Matias et al., 2013).

119 In Morocco, the most seismically active zone is located within the Rif domain (Fig. 1). This
120 regional seismicity is mainly distributed within the upper 30 km of crust, although deeper activity
121 is recorded in the eastern part of the Gibraltar Strait, the western Alboran, and in the Middle Atlas
122 (Hatzfeld & Frogneux, 1981; Cherkaoui, 1991; deVicente et al., 2008; Thiébot & Gutscher, 2006).
123 South of the Rif Mountains, seismicity is significantly more distributed in the Middle Atlas and
124 the High Atlas (Cherkaoui & Medina, 1988; Cherkaoui & Asebriy, 2003; El Alami et al., 1992;
125 Sébrier et al., 2006).

126 In the majority of cases, historical descriptions of Moroccan earthquakes are not sufficiently
127 detailed to precisely evaluate both the epicentral areas and event intensities. El Mrabet (2005)
128 established a reference list of the main historical earthquakes, compiling and analyzing different
129 catalogues (Roux, 1934; Galbis Rodriguez, 1932, 1940; El Alami et al., 1998; Cherkaoui &
130 Asebriy, 2003). In close agreement with the distribution of the instrumental seismicity, these
131 historical events are mainly located in the Tell-Rif Alpine chain (Fig. 1). Along the southern border
132 of the Rif Mountains, the region of Meknès and Fès has experienced almost 10 earthquakes since
133 the eleventh century (Roux, 1934; El Mrabet, 2005; Paláez et al. 2007; Blanc, 2009; Mourabit et
134 al., 2014; Cherkaoui et al., 2017), with three moderate to large events with intensities ranging
135 between VII and VIII in 1045, 1624, and 1755 (Fig. 1). Overshadowed by the large *Lisbon*
136 *Earthquake* in the historical archives (e.g., Blanc, 2009), the precise date of the *Fès-Meknès*
137 *Earthquake* is unclear, with Spanish and Portuguese sources referring to a shock on November 18,
138 which could be interpreted as an aftershock of the *Lisbon Earthquake* (Pereira de Sousa, 1919;
139 Roux, 1934; Vogt, 1984), whereas Arab sources document it on November 27, with an epicentral
140 intensity of VIII that was restricted to the Saïss Region (Moratti et al., 2003; Poujol et al., 2017).



	Space	Time	Dynamics	Techniques
Regional	10-100 km Regional fault?	1-10 Ma Recent fault activity?	Regional dynamics	Regional geodynamic and tectonic maps
Local	1-10 km Fault segmentation?	100 ka-1 Ma Active segments?	Local dynamics	Geological maps, cross-sections, seismic lines, geomorphic analyses
Site	≤1 km Geomorphic cumulative deformation?	≤100 ka Age constraints?	Site dynamics	Geomorphic analyses, cosmogenic dating

141

142 **Figure 2.** (a) Structural map of the main tectonic units composing the Rif Mountains in northern Morocco
 143 (modified after Gimeno-Vives et al., 2020; Suter, 1980; Chalouan et al., 2008), and showing the period of
 144 activity of the main boundary thrusts (after Abbassi et al., 2020). The open box and the red line locate the
 145 map shown in Fig. 3a and the crustal-scale cross-section shown in Fig. 4a, respectively; (b) Principle of
 146 matrix organization used to define a set of diagnostic criteria regarding fault activity in moderate domains
 147 of tectonic deformation. The fourth column lists the different types of data that were used in this study to
 148 cope with the different spatial and temporal scales (adapted from Siame & Sébrier, 2004).

149 **3 Material and Methods**

150 3.1 Diagnostic criteria to identify and characterize moderately active faults in Northern Morocco

151 The search for evidence of fault activity is a long investigation, based on active tectonics,
152 geomorphology, and earthquake geology. Aiming at defining the fault background, it should
153 include not only information on the fault itself but also about its relationships with the
154 seismological and structural environment. Particularly, the fault trace at the surface, as well as its
155 extent, geometry, segmentation, kinematics, and age of activity should be carefully examined
156 together with its relationship with historical and instrumental seismicity.

157 In this study, we rely on the strategy that was defined in the early 2000s by the international
158 consortium involved in the European Project “Slow Active Faults in Europe” (S.A.F.E.; EVG1-
159 2000-22005), and which aimed at reducing the possible misinterpretations in identifying active
160 faults in the context of slowly deforming regions. The determination of such a set of diagnostic
161 criteria is based on a matrix-like, multi-criteria approach (Fig. 2b), which considers that it is key
162 to verify the consistency between the different spatial scales and time windows classically tackled
163 by active tectonic studies. In a simplified manner, the first column of the matrix is interested in the
164 fault existence itself, while the second one is rather focused on the evidence of fault activity at
165 various space scales. The third column deals primarily with the characterization of the fault activity
166 parameters. In a similar way, the first line deals with the regional background of the fault, while
167 the second line mainly concerns fault segmentation, and the third line is interested in more detailed
168 analyses at the site scale (*e.g.*, detailed geomorphic, geophysical studies or paleoseismic trenches).
169 Logical algorithms were developed by the S.A.F.E. project consortium to address basic questions
170 aimed at a correct diagnosis of fault activity (Siame & Sébrier, 2004). The basic content of each
171 matrix box are documents (maps, tables, geological data...) that may be either available from the
172 literature or from new results obtained during the process. The detailed description of each matrix
173 cell box has been released in a deliverable of the S.A.F.E. project (Siame & Sébrier, 2004).

174 3.2 Geomorphic analyses across spatial scales

175 Once the existence of the tectonic features is established at a regional scale (Fig. 3 and Fig. 4), the
176 identification and mapping of fault segments generally rely on morphological and structural
177 analyses of satellite images, aerial photographs, digital terrain models, as well as field

178 observations. This makes it possible to map fault systems from a regional scale (≈ 100 km) to that
179 of the fault segment (≈ 10 km), and to locate sites deserving more detailed field investigations. In
180 this study, we focused on a morpho-chronological approach that requires the preservation of
181 tectonically offset landscape features and datable surfaces that can be used to constrain their age
182 (*e.g.*, Ryerson et al., 2006).

183 To perform a regional survey of the fault system characterizing the front of the Pre-Rif system, a
184 topographical database was built using the Global Digital Surface Model ALOS World 3D
185 (ALOSW3D DSM), with a pixel resolution of 30 m (Takaku et al., 2014, 2018). Ruggedness and
186 topographic position are useful geomorphic tools classically used for landform classification (*e.g.*,
187 Lindsay et al., 2015). To highlight structural and geomorphic features in the studied area (Fig. 3),
188 two grids were derived from the ALOSW3D DSM, emphasizing regional topographic gradients:
189 a map of the multiscale elevation residual index (MERI), and a map of the deviation from mean
190 elevation (DEV). These operations were performed using Whitebox Geospatial Analysis Tools
191 (3.4.0. Montreal version release in 2017; Lindsay, 2016). DEV is the difference between the
192 elevation of the spatial window centre and its mean elevation, normalized by its standard deviation
193 (Gallant & Wilson, 2000). It is a non-dimensional measure of topographic position scaled by the
194 local ruggedness, which is useful in applications where the landscapes of interest are
195 heterogeneous (De Reu et al., 2013). The MERI also characterizes the topographic position but
196 across a range of spatial scales. The algorithm calculates the difference from mean elevation in a
197 series of window sizes from 3×3 to a maximum window size that depends on the size of the DSM.
198 MERI quantifies the proportion of tested scales where the central grid cell has a higher value
199 compared to the mean elevation. Thus, MERI ranges between 0, indicating that a grid cell in a
200 DSM is lower than the mean elevation across the entire range of tested scales, and 1, indicating
201 that the location is consistently higher than the mean elevation (Lindsay, 2016).

202 To downscale the analysis of the fault morphology at the segment scale (≈ 10 km), we used data
203 from the Pléiades constellation, composed of two optical Earth-imaging satellites, which provide
204 very-high-resolution images with multi-stereoscopic potential along the same orbit due to their
205 rapid pointing agility (Bernard et al., 2012). In a sparse vegetation setting such as that of the
206 Meknès and Fès region, Pléiades images are a cost-effective alternative to airborne LiDAR to
207 produce high-resolution DSMs of large areas (*e.g.*, Ansberque et al., 2016).

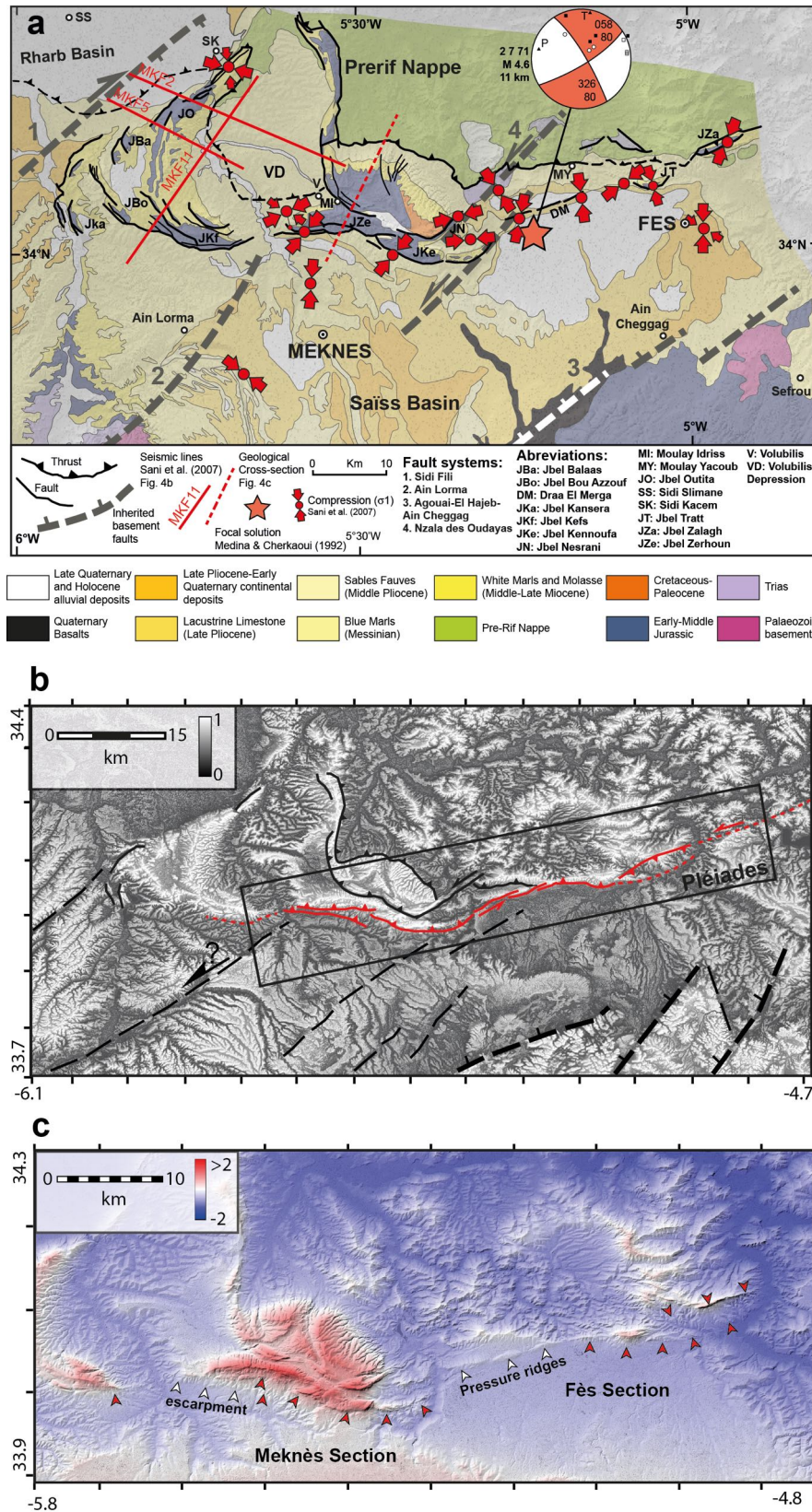
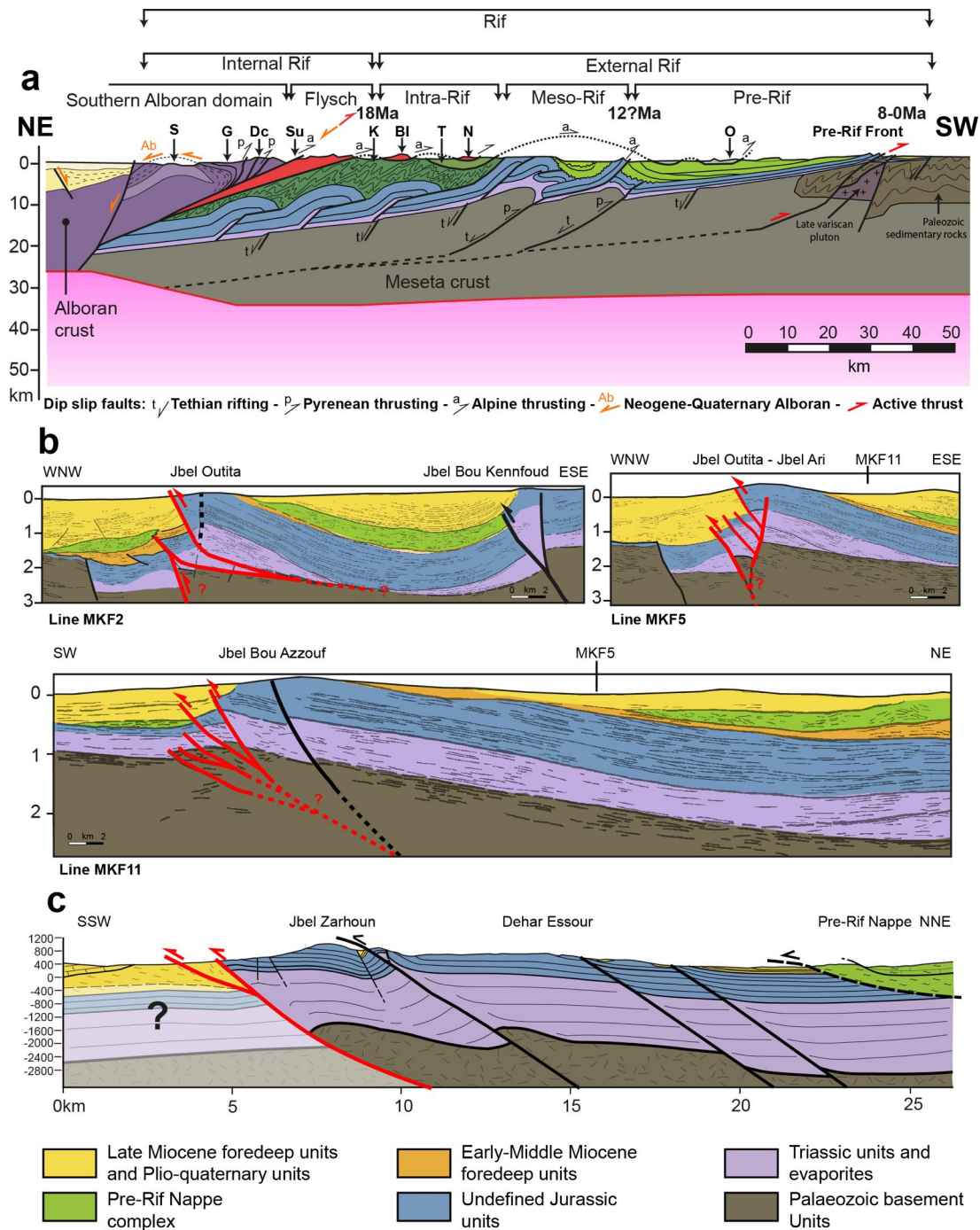


Figure 3. (a) Structural and geological sketch map of the Pre-Rif Ridge at the front of the Pre-Rif Nappe along the northern border of the Saïss Basin (modified after Sani et al., 2007). Red arrows show direction of shortening (after Sani et al., 2007). Solid and dotted red lines locate the seismic lines and geological cross-section depicted in Fig. 4b and Fig. 4c, respectively. Focal mechanism is after Medina & Cherkaoui (1992); (b) Map of the multiscale elevation residual index (MERI) derived from ALOS3D DSM. The prominent tectonic features running along the major relief change are depicted in red. Dashed, solid lines indicate possible surface effect of reactivated basement normal faults. The black open rectangle shows the outlay of the Pleiades images used to survey the fault; (c) Map of the deviation from mean elevation (DEV) derived from ALOS3D DSM. Red arrows indicate prominent geomorphic features running along the major relief change and possibly associated with recent, active tectonic deformation.



209

210 **Figure 4.** (a) Crustal-scale geological cross section extracted from TRANSMED-Transsect I, depicting the main
 211 structures and units between the Alboran Sea and the western Moroccan Meseta (modified after Frizon de
 212 Lamotte et al., 2004). Keys: S, Sebtime; G, Ghomaride; Dc, Dorsale calcaire; Su, Suture of the Maghrebien
 213 Tethys; K, Ketama Unit; T, Tanger Unit; BI/N, Beni Ider and Numidian nappes; O, Ouezzane Unit. Numbers
 214 indicate age of thrusting; (b) Structural interpretation of seismic lines (modified after Sani et al., 2007) with
 215 tentative re-interpretation showing active faults marked in red. Vertical scales in two-way time seconds; (c)
 216 Schematic geological cross-section of Jbel Zarhoun after the 1/50000 geological maps of Sidi Kacem (Bendkik
 217 et al., 2004) and Beni Ammar (Chenakeb et al., 2004), as well as the stratigraphic logs published in Sani et al.
 218 (2007).

219 To encompass the fault system running along the southern front of the Pre-Rif Nappe, we
220 specifically acquired 5 Pléiades stereo-couples along a transect centering the fault zone and
221 covering a total area of 3142 km², with a swath width of 20 km (Fig. 2). The dataset is composed
222 of Pléiades 1B and 1A panchromatic scenes with a resolution of 70 cm, but resampled at a ground
223 sampling distance of 50 cm. The stereoscopic images were then processed to produce a DSM using
224 MicMac photogrammetry open-source software from the French *Institut Géographique National*
225 (Rupnik et al., 2018), and the following workflow pipeline: (1) Satellite images being generated
226 from pushbroom sensors, the geometric model is delivered as Rational Polynomial Coefficients,
227 which is an approximation and needs to be refined; (2) Calculation of the key points on each image
228 with Sift algorithm on sub-sampled images at 5000 pixels width; (3) The refinement of the
229 orientation is performed with polynomial correction functions estimated from bundle block
230 adjustments of the tie points. Ground control points were not used at this step as none were
231 available, yielding an average residual of about 0.5 pixels (and leading to an elevation uncertainty
232 of about 2 m, *e.g.* Panagiotakis et al., 2018); (4) The 3D reconstruction was then done from semi-
233 global multi-view stereo algorithm, pixel to pixel matching from cross-correlation with a moving
234 window of 5x5 pixels size. A threshold of 0.2 for minimum correlation was used to avoid low
235 signal/noise ratio. (5) Finally, the resulting Digital Elevation Model (DEM) was smoothed using a
236 Gaussian filter of 4x4 pixels size. The series of Pléiades images as well as the resulting DEM are
237 shown, together with the structural interpretation, in figure 5.

238 3.3 Placing time constraints using cosmogenic dating

239 In this study, *in situ*-produced ¹⁰Be, ²⁶Al and ³⁶Cl (*e.g.*, Gosse & Philips, 2001; Dunai, 2010) were
240 used to set temporal constraints for the landscape evolution associated with the tectonic activity.
241 In morphochronology, these cosmogenic nuclides are now routinely used as chronometers to
242 extend the time window of fault slip rate estimates obtained by dating landscape features affected
243 by active tectonics. In dating alluvial landforms using cosmogenic nuclides, surface sampling
244 and/or depth profile approaches are two possible options that can be conducted separately or in
245 combination. However, to successfully date alluvial landforms with profiles, the samples must be
246 collected between the surface and a minimum depth of 5 m (*e.g.*, Braucher et al., 2009; Siame et
247 al., 2012). Otherwise, the cosmogenic concentrations are likely to be dominated by the spallogenic
248 (neutrons) component, which is more sensitive to surface processes than the muonic component at

249 depth. In the studied region, Quaternary alluvial deposits are composed of carbonated clasts and
250 are typically less than 3 m-thick. In such conditions, surface sampling was required. *In situ*-
251 produced ^{36}Cl concentrations were measured in surface mudstone cobbles and carbonated
252 sandstone cobbles originating from the Jurassic calcareous formations cropping out in the Pre-Rif
253 Ridges and the Miocene Pre-Rif Nappe, respectively (Suter, 1980). *In situ*-produced ^{10}Be and ^{26}Al
254 concentrations were measured in the quartz isolated from carbonated sandstone cobbles. Prior to
255 chemical procedures, all the samples were crushed and sieved to fractions ranging from 250 and
256 $1000\ \mu\text{m}$.

257 Preparation of *in situ*-produced ^{36}Cl targets for Accelerator Mass Spectrometry (AMS)
258 measurements consists of two hours of water-leaching, followed by a 10%-dissolution using HNO_3
259 ($2\ \text{mol.l}^{-1}$), and a total dissolution in HNO_3 after addition of 2 mg of a ^{35}Cl -enriched carrier
260 ($^{35}\text{Cl}/^{37}\text{Cl}=918$), allowing for simultaneous natural chlorine determination by isotope dilution
261 AMS. For the sandstone cobbles, quartz grains were then recovered from the solution for further
262 ^{10}Be and ^{26}Al procedures. After taking an aliquot for Ca-determination by Inductively Coupled
263 Plasma-Optical Emission Spectrometry, 1 ml of an AgNO_3 solution (10%) was added to the
264 dissolved sample to precipitate AgCl . To reduce isobaric interference by ^{36}S during AMS
265 measurements, the AgCl precipitate was re-dissolved using diluted NH_4OH , and sulphur was co-
266 precipitated with BaCO_3 to form BaSO_4 by addition of an ammoniac saturated $\text{Ba}(\text{NO}_3)_2$ solution.
267 The solution was filtered (acrodisc $0.45\ \mu\text{m}$ filter) and then AgCl was re-precipitated with diluted
268 HNO_3 , washed with water and then dried at 80°C . AMS measurements were performed at the
269 French AMS Facility, ASTER, located at CEREGE in Aix-en-Provence (Arnold et al., 2010). Both
270 the $^{36}\text{Cl}/^{35}\text{Cl}$ and the $^{35}\text{Cl}/^{37}\text{Cl}$ ratios were obtained by normalization to an in-house standard (SM-
271 CL-12) with an assigned $^{36}\text{Cl}/^{35}\text{Cl}$ value of $(1.428\pm 0.021)\times 10^{-12}$ (Merchel et al., 2011; Braucher et
272 al., 2018), and a natural $^{35}\text{Cl}/^{37}\text{Cl}$ ratio of 3.217.

273 For *in situ*-produced ^{10}Be and ^{26}Al , preparation of targets for AMS measurements followed
274 chemical procedures adapted from Brown et al. (1991) and Merchel and Herpers (1999).
275 Decontamination from atmospheric ^{10}Be of the quartz grains included in the carbonated sandstone
276 cobbles was achieved by a series of three successive leachings in concentrated HF ; each leaching
277 removing 10% of the remaining sample mass. Cleaned quartz was then totally digested in
278 concentrated HF , after addition of $100\ \mu\text{g}$ of an in-house carrier at $(3.025\pm 9)\times 10^{-3}\ \text{g/g}$ of ^9Be ,
279 originating from a deep-mined phenakite (Merchel et al., 2008). Hydrofluoric and perchloric

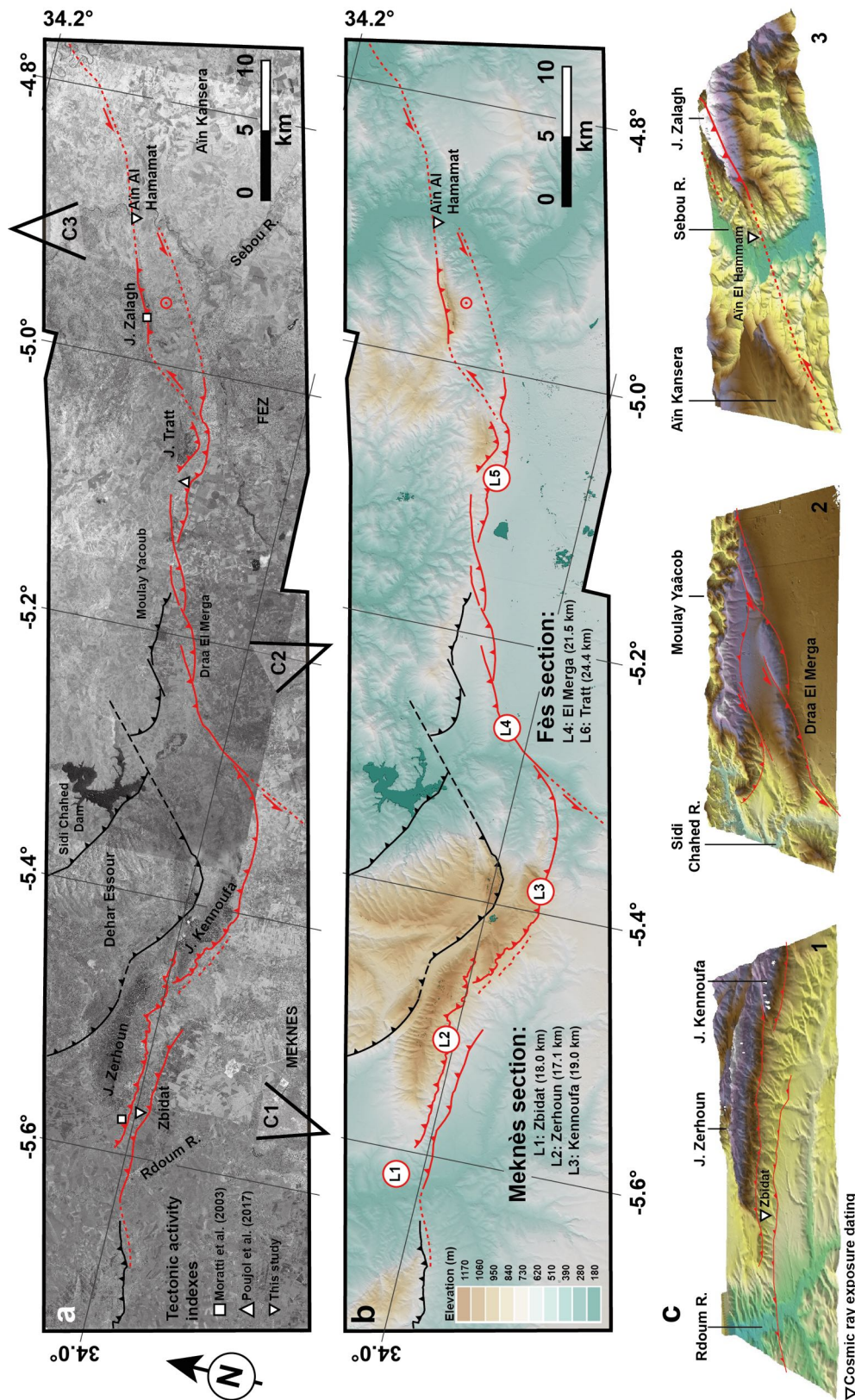


Figure 5. Map of fault traces overlying (a) the mosaic of Pléiades panchromatic scenes specifically acquired in the Fès-Meknès region along the southern Rif deformation front, and (b) the digital surface model (DSM) with 1 m pixel resolution derived from stereoscopic pairs, and showing the main fault segments; (c) 3D bird views extracted from the Pléiades-derived DSM at three specific sites : 1, the Zbidat segment; 2, the El Merga segment; and 3, the termination of the Fès segment, with the Jbel Zalagh pressure ridge. 1 and 2 also locate the sites where the cosmogenic exposure technique has been applied at Zbidat and Ain El Hammam.

281 fuming was used to remove fluorides and both cation and anion exchange chromatography to
282 finally isolate Be and Al. Prior to ^{10}Be and ^{26}Al AMS measurements at ASTER, beryllium and
283 aluminium oxides were mixed to 325-mesh niobium and silver powders, respectively. The ^{10}Be
284 measurements were calibrated against the in-house STD-11 standard
285 ($^{10}\text{Be}/^9\text{Be}=(1.191\pm 0.013)\times 10^{-11}$; Braucher, 2015). Isotopic $^{26}\text{Al}/^{27}\text{Al}$ ratios were measured against
286 the in-house standard SM-Al-11, the $^{26}\text{Al}/^{27}\text{Al}$ value of which $(7.401\pm 0.064)\times 10^{-12}$ has been cross-
287 calibrated against primary standards from a round-robin exercise (Merchel & Bremser, 2004).

288 Reported analytical uncertainties (1σ) include uncertainties in AMS counting statistics, variation
289 of isotopic ratios of standards during the runs, and external AMS uncertainties (Arnold et al., 2010;
290 Braucher et al., 2018). The ^{36}Cl exposure ages were calculated using the Excel® sheet provided
291 by Schimmelpfenning et al. (2009), and a ^{36}Cl sea-level high latitude production rate of
292 42.2 ± 2.0 atoms ^{36}Cl (g-Ca)/yr (Braucher et al., 2011). Exposure ages from ^{10}Be and ^{26}Al
293 concentrations were calculated using a ^{10}Be sea-level high latitude production rate of 4.01 ± 0.33
294 atoms ^{10}Be (g-SiO₂)/yr (Borchers et al., 2016), and half-lives of $(1.387\pm 0.012)\times 10^6$ years
295 (Korschinek et al., 2009; Chmeleff et al., 2009) and $(0.705\pm 0.024)\times 10^6$ years (Nishiizumi et al.,
296 2004, 2007), respectively. For all cosmogenic nuclides, exposure ages were calculated using the
297 time-independent scaling functions for high-energy neutrons of Stone (2000), with an attenuation
298 length of 160 g/cm^2 , and those of Braucher et al. (2011) for muons. A bulk rock density of
299 2.5 g/cm^3 was assumed for all samples. With negligible topographic shielding, all minimum
300 exposure ages were calculated with the “zero erosion” assumption (*e.g.*, Lal, 1991).

301 **4 Appraisal of tectonic activity along the Pre-Rif Ridges**

302 4.1 Regional characteristics of the Pre-Rif deformation front

303 The boundary between the Pre-Rif Ridges and the Saïss Basin has long been investigated through
304 geological (Choubert & Faure-Muret, 1962; Faugères, 1978; Morel 1988, 1989), structural
305 (Bargach et al., 2004; Frizon de Lamotte et al., 2004; Moratti et al., 2003; Sani et al., 2007), and
306 geodetic (Chalouan et al., 2014; Poujol et al., 2017) approaches. The Pre-Rif Ridges correspond
307 to elongated hills of Mesozoic sedimentary rocks that belong to the Meseta-Atlas cover of the
308 foreland involved in the Late Miocene to Middle Pliocene thrusting of the external Rif (Faugères,
309 1978; Zizi, 1996).

310 To the west of the Volubilis Depression (Fig. 3), the external Pre-Rif Ridges (Jbel Bou Draa,
311 Outita, Balaas, Kansera, Bou Azzouf, Kefs) form a westward convex, arched-like morphology
312 marking the limit with the Rharb Basin (Bargach et al., 2004), which is probably limited at depth
313 by the NE-striking Sidi Fili fault system (e.g., Sani et al., 2007). To the east of the Volubilis
314 Depression, the internal Pre-Rif Ridges (Jbel Tselfat, Bou Kannfoud, Zerhoun, Kennoufa, Nesrani)
315 form another though wider southward convex, arched-like morphology (Bargach et al., 2004).
316 Further east, along the Pre-Rif deformation front, two insulated ridges (Jbel Tratt and Zalagh) stand
317 on both sides of Fès City (Fig. 3).

318 The ridges are made of a sedimentary sequence that starts with Triassic evaporites and red clays
319 overlain by a relatively thick Jurassic series of dolomite and limestone, and locally by a marly
320 Cretaceous formation in the eastern ridges (Bargach et al., 2004). The Mesozoic cover is
321 unconformably overlain by Lower and Middle Miocene marls as well as Middle-Upper Miocene
322 sandstones (Fig. 3 & 4). From a structural point of view, these deposits generally correspond to
323 SW- and S-verging anticlines associated with the thrusting of the Pre-Rif Nappe, and deforming
324 the Rharb and Saïss Neogene basins, respectively (Fig. 3 & 4).

325 At a regional scale, the morphology associated with the Pre-Rif Ridges is particularly highlighted
326 by the MERI and DEV maps derived from the ALOS3D digital surface model (Fig. 3). The
327 DEV map brings out the major geomorphic features associated with the activity of the faults (fault
328 traces, topographic escarpments, en-échellon pressure ridges...). The MERI map allows mapping
329 the fault geometry and broadly defining the segmentation of the Pre-Rif deformation front into two
330 Meknès and Fès sections. At a first order, this segmentation appears controlled by the interaction
331 between the Pre-Rif thrusts and the NE-striking basement faults below the Mesozoic cover
332 (Fig. 3). The Sidi Fili fault system delimits the Khemisset Basin to the northwest (Fig. 3 and
333 Fig. 4). The Ain Lorma fault system marks the southeastern shoulder of the Khemisset Basin, and
334 marks the limit between the external and internal Pre-Rif Ridges (e.g., Suter, 1980). According to
335 the seismic lines interpreted by Sani et al. (2007), the Ain Lorma fault system does not affect the
336 sedimentary deposits overlying the basal part of the Neogene sediment. Nevertheless, the NE-SW
337 linear pattern in the Saïss Basin morphology, evidenced by the MERI map, might well be an
338 evidence of some structural control within the most recent deposits (Fig. 3). The Nzala des
339 Oudayas fault system delimits the internal Pre-Rif Ridges to the east of Jbel Kennoufa and Jbel
340 Nesrani, marking the limit between the Meknès and Fès sections of the fault zone (Fig. 3 and 5).

341 This fault system is evidenced by an alignment of Triassic evaporites, and the curvature of the Pre-
342 Rif Nappe front in this area (Fig. 3). It also corresponds to the direction of a series of en-échelon
343 pressure ridges, aligned along the Draa El Merga (*e.g.*, Poujol et al., 2017), that are well identified
344 on the DEV map (Fig. 3). All these basement faults are clearly imaged on the seismic profiles
345 published by Sani et al. (2007), and characterized by both a sudden increase of the Mesozoic
346 sediment thickness and a basement involvement in the deformation (Fig. 4).

347 Although the Pre-Rif Ridges probably started to develop in the Early Miocene, the most active
348 phase of compression occurred during the Pliocene, with a direction of maximum compression
349 oriented roughly N-S to NE-SW (Fig. 3), and a reactivation of the earlier basement, normal faults
350 delimiting the Mesozoic grabens as strike-slip faults (Bargach et al., 2004; Sani et al., 2007). Using
351 GPS measurements and block models (Fadil et al., 2006; Vernant et al., 2010; Koulali et al., 2011),
352 Poujol et al. (2017) estimated that the Pre-Rif front should accommodate a shortening and a left-
353 lateral motion at rates of about 4 and 2 mm/yr, respectively. Chalouan et al. (2014) also suggested
354 that this convergence should be accommodated by ENE-striking, northward-dipping reverse and
355 left-lateral faults, as well as south-verging folds. Along the Pre-Rif front, the only focal mechanism
356 solution available is that of a M 4.6 earthquake, which was recorded on July, 2nd 1971, close to
357 Moulay Yacob (Fig. 3). Felt with an intensity of V (MSK), the focal solution depicts left-lateral
358 and right-lateral displacements along N326- and N58-striking planes, respectively (Medina &
359 Cherkaoui, 1992). This is exactly the opposite of what would be expected given the geometry of
360 the faults, and the pattern of maximum compression (Fig. 3). This contradiction is probably due to
361 the lack of data in the south and west quadrants (Medina & Cherkaoui, 1992). Even if the focal
362 depth of 11 km-deep estimated for this seismic event may be somewhat erroneous, it is worth
363 noting that it is compatible with a slip in the basement and not in the Mesozoic sedimentary cover.

364 4.2 Segmentation of the Pre-Rif deformation front

365 Geomorphic and structural analyses were carried out along the Pre-Rif Ridges within the region
366 of Meknès and Fès through a detailed mapping of geomorphic markers, using the DSM extracted
367 from the Pléiades stereoscopic scenes and field surveys. Mapping of the geomorphic indicators
368 enabled us to identify and connect several fault segments along the whole fault system, from the
369 westernmost tip of Jbel Zerhoun to Aïn Kansera Plateau to the east (Fig. 5). This analysis also
370 permitted us to locate two specific sites of detailed morphochronological investigations (see 4.3)

371 at the toe of Jbel Zerhoun, along the Meknès Section, and to the northeast of Fès City, in the
372 pressure-ridge of Jbel Zalagh (Fig. 5).

373 At the toe of Jbel Zerhoun and Jbel Kennoufa, the Pléiades-derived DSM confirms the clear trace
374 of the underlying thrust through the morphology, materialized by two ENE-striking segments of
375 17 and 18 km-long, respectively (Fig. 5). To the west of Jbel Zerhoun, the fault trace is not visible,
376 probably limited at depth by the Ain Lorma basement fault system. To the east of Jbel Kennoufa,
377 the fault trace runs in the Plio-Quaternary sediments, and curves into a more NE-striking direction,
378 parallel to the structural direction of the Nzala des Oudayas basement fault system (Fig. 5).

379 Beside these two thrust segments, another geomorphic evidence of recent fault activity is a
380 topographic escarpment located to the south of Jbel Zerhoun and north of Rdoum River (Fig. 5).
381 In this area, the surface of the Holo-Pleistocene alluvial plain that skirts the toe of the ridge is
382 warped, and exhibits a cumulated topographic escarpment up to 38 m-high (Fig. 6). This
383 topographic feature is suggested in the morphology by a series of aligned, renewed gullies
384 generated by backward erosion, strongly suggesting a recent uplift activity (Fig. 6). This 14 km-
385 long topographic escarpment can be morphologically traced from the eastern tip of Jbel Zerhoun,
386 although subdued features on the DSM may suggest that it continues up to the eastern tip of the
387 Jbel Kefs, which would extend its length to a maximum of 18 km (Fig. 5). Further east, the
388 topographic escarpment fades away, and the DSM does not exhibit clear features beside a few
389 linear traces, limited in length, and without direct connection to the Zbidat escarpment (Fig. 5).
390 Based on this morphotectonic analysis, the Pre-Rif front along the Meknès Section can thus be
391 divided into three main reverse segments: Zerhoun (17 km) and Kennoufa (18 km), running at the
392 toe of the carbonated relief, and Zbidat (14-18.5 km), which is marked by the prominent, 38 m-
393 high topographic escarpment warping the more recent alluvial deposits (Fig. 5).

394 To the east of Jbel Kennoufa, the Fès Section is connected to the Meknès Section by the NE-SW
395 trending, ≈ 22 km-long, the El Merga strike-slip segment that parallels the trend of the Nzala des
396 Oudayas basement fault system and connects to a series of aligned, en échelon elongated hills
397 (Fig. 5). As already indicated by Poujol et al. (2017), this series of low hills are composed of Plio-
398 Quaternary sediments and associated with laterally offset streams. To the east, this segment
399 connects to the front of the Pre-Rif Nappe, resulting in the maximum 24.4 km-long reverse Tratt
400 segment that runs along the piedmont of the main relief, north of Fès City, to the southern slopes

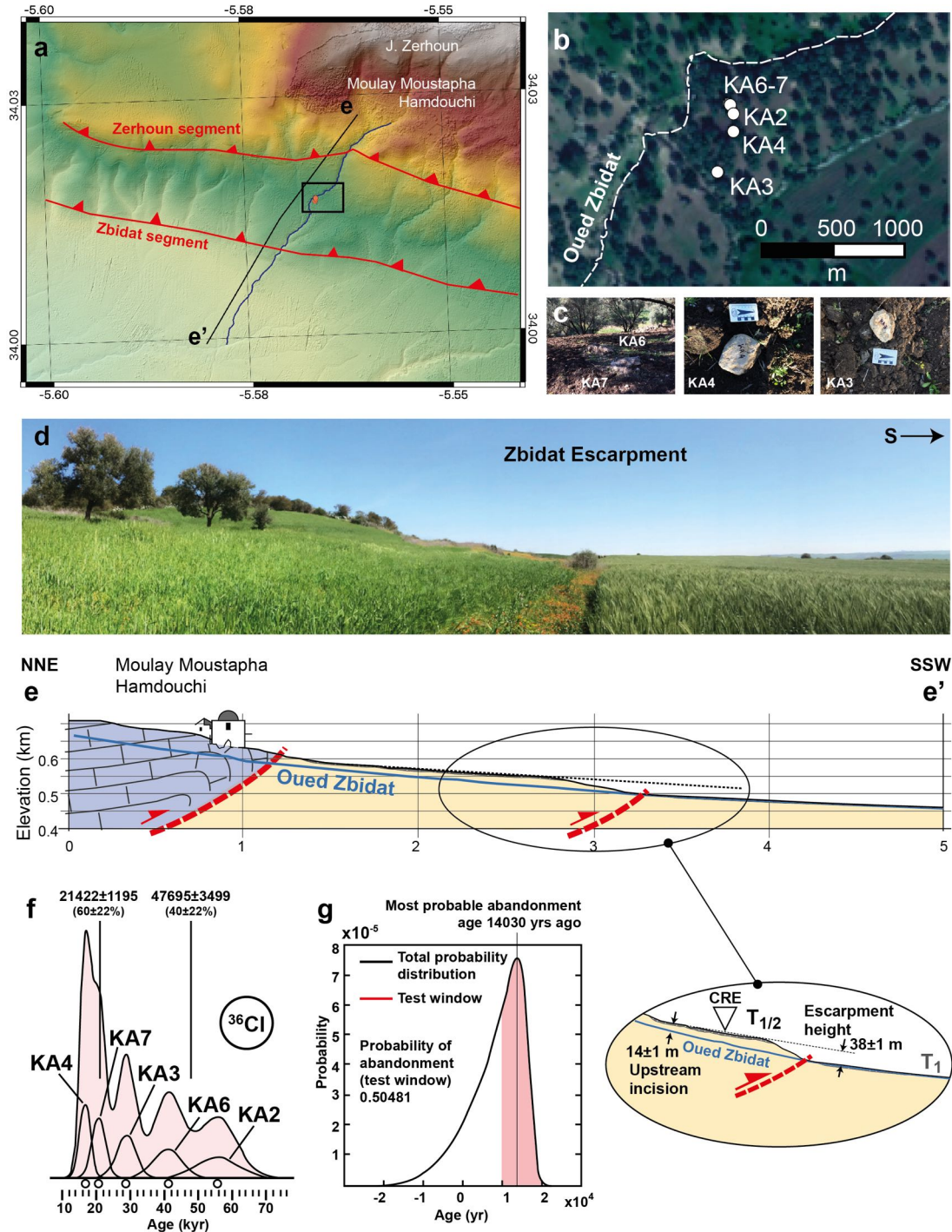
401 of the Jbel Zalagh. To the east, the subdued fault trace running through the southern hillslopes of
402 Jbel Zalagh does not seem to cross the Sebou River (Fig. 5).

403 Conversely, the northern slopes of the Jbel Zalagh are affected by a clearer, linear, left-lateral and
404 reverse fault trace (*e.g.*, Poujol et al., 2017), suggesting that relief surrounding Jbel Zalagh might
405 well be interpreted as a restraining ridge between the Tratt segment and the continuation of the
406 Pre-Rif front further east (Fig. 5). Along the Fès section, the Pre-Rif front is thus mainly composed
407 of the left-lateral El Merga (22 km) and reverse Tratt (24 km) segments, making this portion of the
408 front a zone of relatively more localized deformation than the Meknès Section.

409 4.3 Temporal constraints on geomorphic evolution at the site scale

410 Along the Meknès and Fès sections (Fig. 5), two sites were selected to apply a
411 morphochronological approach using *in situ*-produced cosmogenic nuclides. In Zbidat, the target
412 morphology corresponds to a Quaternary alluvial surface sitting atop of the 38-m high escarpment
413 running at the toe of the Jbel Zerhoun (Fig. 6). Dating the abandonment period of this surface
414 constrains the incision rates of the intermittent rivers running across the escarpment, and thus gives
415 a proxy for the local uplift rate associated with the Zbidat segment. In Aïn Al Hamamat, the target
416 morphology corresponds to a series of stepped fluvial terraces that were abandoned by the Sebou
417 River during uplift in the area of the Jbel Zalagh pressure-ridge (Fig. 7). Dating the abandonment
418 periods of these fluvial terraces constrains incision rates for the Sebou River, where it crosses the
419 front of the Pre-Rif Nappe, and gives a proxy for the regional uplift rate associated with the
420 deformation front.

421 In both sites, the geomorphic surfaces are slightly affected by traditional non-mechanical
422 agriculture, with a maximum ploughing depth of 30 cm. They are also poor in large, stable surface
423 boulders that are less prone to post-depositional disturbances. Due to this lack of boulders, surface
424 sampling was thus limited to cobbles or large pebbles exceeding 10 cm in diameter. In Zbidat, the
425 surface sampling consisted of three calcareous cobbles and two small boulders that have been
426 chiseled in their topmost part. In Aïn Al Hamamat, the surface sampling consisted of 19 cobbles
427 and pebbles of carbonate or carbonated sandstone (Table 1).



428
 429 **Figure 6.** (a) Extract of the Pléiades-derived DSM centered on the Meknès Section and showing the Zbidat
 430 escarpment as well as the Zerhoun segment; (b) Localization of the surface samples for cosmic ray exposure
 431 dating (Tables 2 & 3); (c) Field photographs of selected samples in their original positions; (d) Field photograph
 432 looking eastwardly, showing the topographic escarpment at Zbidat; (e) Topographic cross-section (surface and
 433 stream bed) across the escarpment up to the Zerhoun segment, extracted from the Pléiades-derived DSM. The
 434 inset shows the upstream incision and escarpment height of 14 ± 1 m and 38 ± 1 m, respectively; (f) Cosmogenic
 435 exposure dating (^{36}Cl) shown as probability distribution curves and χ^2 -test peak ages (Table 4); (g) Probability
 436 distribution of abandonment age calculated using the MATLAB tool provided by D'Arcy et al. (2019) over a
 437 11-22 kyr time window.

438

439 Table 1. List of carbonate (carb.) and stanstone (sandst.) surface samples for cosmic ray exposure dating. Scaling factors (S.F.) for
 440 spallogenic (sp) and muonic (m) contributions are calculated after Stone (2000) and Braucher et al. (2011), respectively.

Sample Id	Size/ lithology	Location	Geomorphic position	Lat. (WGS84)	Lon. (WGS84)	Elevation (m)	Atm. Pressure (mbar)	S.F sp	S.F m	Po ¹⁰ Be (atoms/g/yr)	Po ²⁶ Al (atoms/g/yr)	Po ³⁶ Cl (atoms/g/yr)
KA2	pebble/carb.	Zbidat	T1/T2	34.0143	-5.5661	474	958	1.29	1.24	-	-	24.7 ± 2.1
KA3	pebble/carb.	Zbidat	T1/T2	34.0140	-5.5662	472	958	1.28	1.24	-	-	27.3 ± 2.3
KA4	pebble/carb.	Zbidat	T1/T2	34.0142	-5.5661	472	958	1.28	1.24	-	-	28.1 ± 2.3
KA6	boulder/carb	Zbidat	T1/T2	34.0143	-5.5661	477	957	1.29	1.24	-	-	26.2 ± 2.1
KA7	boulder/carb	Zbidat	T1/T2	34.0143	-5.5661	477	957	1.28	1.24	-	-	29.5 ± 2.4
KA8	cobble/carb.	Hamamat	T3	34.1205	-4.9009	279	980	1.10	1.14	-	-	25.9 ± 2.1
KA9	cobble/carb.	Hamamat	T3	34.1207	-4.9010	279	980	1.10	1.14	-	-	27.8 ± 2.1
KA10	boulder/sandst.	Hamamat	T3	34.1209	-4.9014	281	980	1.11	1.14	-	-	26.2 ± 2.0
KA11	cobble/sandst.	Hamamat	T3	34.1214	-4.9017	283	980	1.11	1.14	-	-	26.7 ± 2.1
KA12-3	pebble/sandst.	Hamamat	T3	34.1216	-4.8997	274	981	1.10	1.13	4.4 ± 0.3	29.2 ± 1.8	38.4 ± 2.8
KA12-4	pebble/sandst.	Hamamat	T3	34.1216	-4.8997	274	981	1.10	1.13	4.4 ± 0.3	29.2 ± 1.8	27.1 ± 2.1
KA13	cobble/carb.	Hamamat	T2	34.1202	-4.8980	261	982	1.09	1.13	-	-	23.5 ± 2.0
KA14	cobble/sandst.	Hamamat	T2	34.1202	-4.8979	261	982	1.09	1.13	4.4 ± 0.3	28.9 ± 1.7	24.1 ± 2.0
KA15	cobble/sandst.	Hamamat	T2	34.1202	-4.8980	261	982	1.09	1.13	4.4 ± 0.3	28.9 ± 1.7	26.7 ± 2.1
KA16	cobble/carb.	Hamamat	T2	34.1201	-4.8980	261	982	1.09	1.13	-	-	38.5 ± 2.5
KA17	cobble/sandst.	Hamamat	T2	34.1201	-4.8980	261	982	1.09	1.13	-	-	25.3 ± 2.0
KA18	cobble/carb.	Hamamat	T2	34.1202	-4.8980	261	982	1.09	1.13	-	-	27.4 ± 2.1
KA19	cobble/sandst.	Hamamat	T1	34.1218	-4.8966	233	986	1.06	1.11	4.3 ± 0.3	28.3 ± 1.7	23.7 ± 2.0
KA20	cobble/carb.	Hamamat	T1	34.1218	-4.8966	233	986	1.06	1.11	-	-	32.6 ± 2.4
KA21	pebble/carb.	Hamamat	T1	34.1219	-4.8967	233	986	1.06	1.11	-	-	27.8 ± 2.1
KA22	pebble/sandst.	Hamamat	T1	34.1219	-4.8967	233	986	1.06	1.11	4.3 ± 0.3	28.3 ± 1.7	22.3 ± 1.9
KA23	cobble/carb.	Hamamat	T1	34.1222	-4.8967	233	986	1.06	1.11	-	-	25.4 ± 2.0

441

442 Table 2. *In situ*-produced ^{36}Cl concentrations and associated minimum cosmic ray exposure ages at Zbidat and Ain El Hamamat.

443

Sample Id	Location	Geomorphic position	Mass of dissolved rock (g)	Cl (ppm)	Ca (wt%)	Mg (wt%)	$^{36}\text{Cl}/^{35}\text{Cl}$ ($\times 10^{-13}$)	$[\text{}^{36}\text{Cl}]$ ($\times 10^6$ atoms/g)	Min. ^{36}Cl age (yr)	Max. ^{36}Cl denudation rate (m/Myr)
KA2	Zbidat	T1/T2	65.97	68.7	34.0	0.6	9.10 ± 0.39	1.292 ± 0.067	$55\,615 \pm 5\,796$	-
KA3	Zbidat	T1/T2	78.76	9.4	54.4	0.0	13.36 ± 0.59	0.759 ± 0.034	$28\,801 \pm 2\,843$	-
KA4	Zbidat	T1/T2	70.77	21.9	54.1	0.0	5.93 ± 0.26	0.461 ± 0.021	$16\,758 \pm 1\,605$	-
KA6	Zbidat	T1/T2	72.30	76.1	36.4	0.5	7.02 ± 0.31	1.027 ± 0.058	$41\,036 \pm 4\,232$	-
KA7	Zbidat	T1/T2	69.73	35.1	55.3	0.0	6.26 ± 0.27	0.597 ± 0.028	$20\,732 \pm 1\,978$	-
KA8	Hamamat	T3	59.85	55.4	51.7	0.0	3.93 ± 0.18	0.511 ± 0.032	$20\,236 \pm 2\,117$	77.2 ± 6.7
KA9	Hamamat	T3	58.60	176.4	29.4	0.6	1.72 ± 0.11	0.493 ± 0.058	$18\,089 \pm 2\,608$	86.6 ± 11.5
KA10	Hamamat	T3	70.41	128.2	35.3	0.5	0.54 ± 0.07	0.114 ± 0.021	$4\,375 \pm 892$	363.8 ± 71.6
KA11	Hamamat	T3	72.48	131.4	36.3	0.4	1.02 ± 0.08	0.221 ± 0.029	$8\,328 \pm 1\,294$	190.3 ± 27.8
KA12-3	Hamamat	T3	27.62	334.3	28.8	0.3	2.75 ± 0.16	1.530 ± 0.177	$41\,743 \pm 6\,029$	36.5 ± 4.8
KA12-4	Hamamat	T3	41.18	73.8	51.9	0.0	6.01 ± 0.31	1.083 ± 0.066	$42\,005 \pm 4\,392$	36.3 ± 3.1
KA13	Hamamat	T2	77.06	24.4	51.5	0.0	14.57 ± 0.69	1.125 ± 0.063	$50\,695 \pm 5\,458$	-
KA14	Hamamat	T2	38.46	33.4	51.3	0.0	9.27 ± 0.40	1.243 ± 0.059	$54\,892 \pm 5\,612$	-
KA15	Hamamat	T2	27.33	78.4	50.6	0.0	4.81 ± 0.25	1.101 ± 0.062	$43\,653 \pm 4\,399$	-
KA16	Hamamat	T2	61.03	345.7	28.6	0.6	3.19 ± 0.18	1.603 ± 0.361	$43\,653 \pm 10\,877$	-
KA17	Hamamat	T2	56.98	53.8	51.3	0.0	5.54 ± 0.26	0.724 ± 0.042	$29\,583 \pm 3\,056$	-
KA18	Hamamat	T2	62.98	181.7	28.6	0.6	3.82 ± 0.20	1.105 ± 0.150	$42\,175 \pm 6\,911$	-
KA19	Hamamat	T1	18.04	39.4	50.2	0.0	3.70 ± 0.19	0.908 ± 0.048	$40\,154 \pm 4\,155$	-
KA20	Hamamat	T1	62.03	268.5	28.3	0.6	2.60 ± 0.15	1.042 ± 0.206	$33\,205 \pm 7\,306$	-
KA21	Hamamat	T1	64.19	197.1	28.4	0.6	1.91 ± 0.12	0.586 ± 0.101	$21\,559 \pm 4\,180$	-
KA22	Hamamat	T1	34.15	33.3	46.9	0.1	9.56 ± 0.42	1.392 ± 0.065	$67\,329 \pm 7\,100$	-
KA23	Hamamat	T1	62.98	158.9	28.8	0.6	3.59 ± 0.19	0.933 ± 0.111	$38\,316 \pm 5\,725$	-

444 Note: Samples KA2 to KA7 were processed together with a blank sample yielding a $^{36}\text{Cl}/^{35}\text{Cl}$ ratio of $(3.63 \pm 0.94) \times 10^{-15}$.

445 The others were processed with another blank sample yielding a $^{36}\text{Cl}/^{35}\text{Cl}$ ratio of $(2.65 \pm 0.89) \times 10^{-15}$.

446

447

448

449 Table 3. *In situ*-produced ^{10}Be and ^{26}Al concentrations and associated minimum cosmic ray exposure ages at Aïn El Hamamat.

450 Exposure ages are calculated neglecting muonic contribution at the surface as it accounts for less than 3% of the total production.

Sample Id	Mass of quartz (g)	Mass of spike ^9Be (g)*	$^{26}\text{Al}/^{27}\text{Al}$ ($\times 10^{-13}$)	$[^{26}\text{Al}]$ ($\times 10^6$ atoms/g)	Min. ^{26}Al age (yr)	$^{10}\text{Be}/^9\text{Be}$ ($\times 10^{-13}$)	$[^{10}\text{Be}]$ ($\times 10^6$ atoms/g)	Min. ^{10}Be age (yr)	$^{26}\text{Al}/^{10}\text{Be}$
KA12-3 / T3	27.19	0.1511	15.05 ± 0.5	4.098 ± 0.144	$150\,732 \pm 10\,483$	6.24 ± 0.25	0.698 ± 0.029	$164\,407 \pm 11\,950$	5.9 ± 0.3
KA12-4 / T3	20.07	0.1523	2.05 ± 0.15	1.488 ± 0.111	$52\,183 \pm 4\,987$	2.61 ± 0.11	0.396 ± 0.017	$91\,574 \pm 6\,725$	3.8 ± 0.3
KA14 / T2	13.34	0.1519	8.53 ± 0.47	1.872 ± 0.100	$66\,829 \pm 5\,358$	1.60 ± 0.08	0.362 ± 0.018	$84\,473 \pm 6\,604$	5.2 ± 0.4
KA15 / T2	26.55	0.1539	3.75 ± 0.22	1.080 ± 0.063	$38\,012 \pm 3\,189$	1.63 ± 0.07	0.188 ± 0.008	$43\,481 \pm 3\,200$	5.7 ± 0.4
KA19 / T1	26.12	0.1525	3.25 ± 0.22	0.982 ± 0.066	$35\,337 \pm 3\,178$	1.43 ± 0.07	0.166 ± 0.009	$39\,186 \pm 3\,111$	5.9 ± 0.5
KA22 / T1	7.22	0.1530	5.92 ± 0.30	4.333 ± 0.224	$166\,103 \pm 13\,146$	2.29 ± 0.11	0.964 ± 0.046	$239\,061 \pm 18\,300$	4.5 ± 0.3
Blank	-	0.1530	$<2.76 \times 10^{-15}$	-	-	$(2.37 \pm 0.32) \times 10^{-15}$	-	-	-

451 Note: ^{10}Be and ^{26}Al were performed at ASTER AMS facility (Aix-en-Provence, France). BeO machine blank $^{10}\text{Be}/^9\text{Be}$ ratio is 3.55×10^{-16} . Al_2O_3 452 machine blank $^{26}\text{Al}/^{27}\text{Al}$ ratio is 2.95×10^{-15} . * in-house carrier at $(3.025 \pm 9) \times 10^{-3}$ g/g of ^9Be ; No ^{27}Al spike was added.

453

454

455 For the two sampled sites, the measured *in situ*-produced cosmogenic ^{36}Cl concentrations yield a
456 rather well-distributed dataset of minimum exposure ages (Table 2 & 3). In addition, some samples
457 are characterized by a high content in ^{35}Cl (above 100 ppm), which could represent a significant
458 source of uncertainty because of the poorly constrained fluxes of thermal and epithermal neutrons
459 that produce ^{36}Cl through neutron capture (Schimmelpfenning et al., 2009; Delunel et al., 2014).
460 The exposure ages determined for these high ^{35}Cl samples might be overestimated and should be
461 regarded with caution (e.g., Moulin et al., 2016; Rizza et al., 2019). To help improve the
462 interpretation, probability density plots were derived using DensityPlotter, a java application
463 originally designed to interpret populations of single grains from fission track or luminescence
464 dating (Vermeesch, 2012). For each group of cosmogenic exposure ages, a χ^2 -test was employed
465 to determine whether their distribution is statistically homogeneous (Table 4). This procedure also
466 determines if the age populations contain more than one mode, yielding in this case mixture age
467 models accounting for both analytical and statistical dispersion (Galbraith & Green, 1990).

468 For the samples collected on the alluvial surface hanging above the Zbidat escarpment, ^{36}Cl
469 concentrations are ranging from $(0.46\pm 0.02)\times 10^6$ to $(1.29\pm 0.07)\times 10^6$ atoms.g $^{-1}$, with relatively low
470 natural chlorine concentrations (Table 2). These ^{36}Cl concentrations yield minimum exposure ages
471 comprised between 16.8 ± 1.6 and 55.6 ± 5.8 ka (Table 2). For these age population, the probability
472 distribution curve is positively-skewed toward older exposure ages (Fig. 6), with two principal
473 peaks centred at 21.4 ± 1.2 and 47.7 ± 3.5 ka, and a central value at 29.6 ± 5.8 ka with 43% of
474 dispersion (Table 4).

475 In Aïn Al Hamamat, measured ^{36}Cl concentrations range from $(0.11\pm 0.02)\times 10^6$ to $(1.39$
476 $\pm 0.07)\times 10^6$ atoms.g $^{-1}$, yielding minimum cosmogenic exposure ages comprised between 4.4 ± 0.9
477 and 67.3 ± 7.1 ka (Table 2). For each alluvial surface, a couple of carbonated sandstones also
478 enabled measurements of *in situ*-produced cosmogenic ^{10}Be and ^{26}Al concentrations (Table 3). In
479 these peculiar samples, ^{10}Be and ^{26}Al concentrations ranged from $(0.17\pm 0.01)\times 10^6$ to
480 $(0.96\pm 0.05)\times 10^6$ atoms.g $^{-1}$, respectively (Table 3). These ^{10}Be and ^{26}Al concentrations yield
481 minimum exposure ages comprised between 35.3 ± 3.2 and 239.1 ± 18.3 ka (Table 3). For the three
482 alluvial surfaces, the age distribution patterns indicate that minimum exposure ages derived from
483 ^{10}Be and ^{26}Al concentrations are generally older than those derived from ^{36}Cl concentrations
484 (Tables 2 and 3).

485

486

487

488

Table 4. Statistical χ^2 -tests performed using DensityPlotter (Vermeesch, 2012) and most probable abandonment ages using the probabilistic approach of D'Arcy et al. (2019)

489

Group of samples	Geomorphic position	Number of samples	Central value years (1σ)	Dispersion	$P(\chi^2)$	Peak 1 Years (1σ)	Peak 2 Years (1σ)
Zbidat	T1/T2	5	29 582 \pm 5 780	0.43	0.00	21 423 \pm 1 195 (60%)	47 695 \pm 3 499 (40%)
Hamamat	T2	6	43 338 \pm 3 976	0.18	0.00	29 861 \pm 3 202 (18%)	48 308 \pm 2 659 (82%)
Hamamat	T1	4	33 751 \pm 3 898	0.17	0.04	22 098 \pm 4 744 (26%)	38 602 \pm 3 157 (74%)

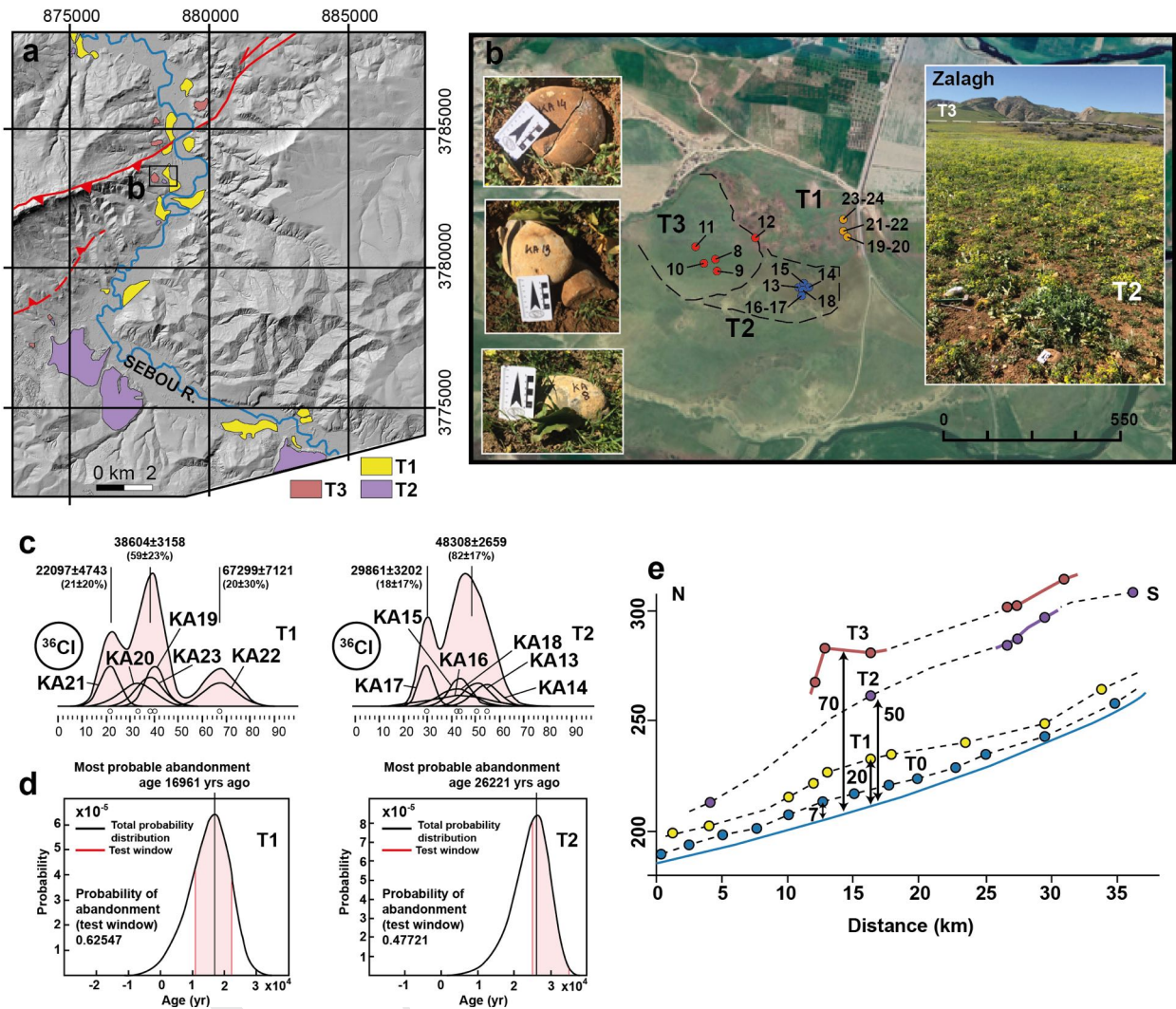
490

491

492

493

494



495

496

497 **Figure 7.** (a) Extract of the Pléiades-derived DSM centered on the Sebou River, east of Fès City, and
 498 showing the distribution of the alluvial terraces along the river; (b) Google Earth image extract of Aïn Al
 499 Hamamat area showing the position of the samples from the three alluvial surfaces (Tables 1, 2, and 3).
 500 Field photographs show the general morphology of terrace T2 (with T3 in the background) as well as some
 501 of the samples in their original position; (c) Cosmogenic exposure dating (^{36}Cl) for T1 and T2 shown as
 502 probability distribution curves and χ^2 -test peak ages (Table 4); (d) Probability distributions of abandonment
 503 ages for T1 and T2, calculated using the MATLAB tool provided by D'Arcy et al. (2019) over a time window
 504 of 11-22 kyr and 25-35 ka, respectively; (e) Vertical distribution of the alluvial terraces along the Sebou
 505 River and estimation of the vertical incision at Aïn Al Hamamat. Elevation points were sampled on the
 506 Pléiades-derived DSM.

507

508

509

510 For the lowest terrace (T_1), the probability distribution of minimum exposure ages derived from
511 ^{36}Cl concentrations is mono-modal (Fig. 7), with a central value of 36.7 ± 2.0 ka, which is consistent
512 with the minimum exposure ages derived for one carbonated sandstone (KA19) using ^{10}Be and
513 ^{26}Al concentrations (Tables 2 & 3).

514 For the middle terrace (T_2), measured ^{36}Cl concentrations yield a majority of the samples agreeing
515 with a minimum exposure age of 48.3 ± 2.7 ka (Fig. 7), which is also in relative good agreement
516 with the minimum exposure ages derived for one carbonated sandstone (KA15) using ^{10}Be and
517 ^{26}Al concentrations (Tables 2 & 3). For this population of samples, the χ^2 -test also accepts a
518 younger peak at 29.9 ± 3.2 ka, which however relies on only one sample (KA17). Among the
519 samples collected on the middle terrace, two are characterized by high ^{35}Cl contents (KA16 and
520 KA18), and should thus be interpreted with caution.

521 For the upper terrace (T_3), the measured ^{36}Cl concentrations yield minimum exposure ages that are
522 younger than those obtained for the two other alluvial surfaces (Table 3). This is counter-intuitive
523 since the highest terrace is expected to be the oldest. An alternative interpretation is to consider
524 that this higher alluvial surface has already achieved the cosmogenic steady-state for spallation
525 production pathway (e.g., Lal, 1991). The measured ^{36}Cl concentrations may thus reflect the local
526 denudation rate acting on such alluvial material (Table 2). Besides two samples that are
527 characterized by significantly lower ^{36}Cl concentrations (KA10 and KA11), the others agree on
528 surface lowering rates ranging from 36 ± 3 to 87 ± 12 m/Ma (Table 2). However, most of them are
529 also characterized by high ^{35}Cl contents, and these estimates should thus be considered with
530 caution.

531 **5 Discussion**

532 5.1 Significance of the cosmogenic exposure ages

533 Conversely to the sandstone coming from the Miocene Pre-Rif Nappe, the carbonate cobbles are
534 derived from more local Jurassic formations that crop out in the Pre-Rif Ridges (Suter, 1980).
535 Indeed, the Sebou watershed is roughly 6500 km^2 in area upstream of Aïn Al Hamamat, with large
536 fluvial terraces along the river bed (Fig. 7). This situation left many opportunities for the sandstone
537 cobbles to experience complex exposure scenarios with alternating burial/exposure episodes
538 during transport. The pair of *in situ*-produced ^{10}Be and ^{26}Al has long been proposed for studying

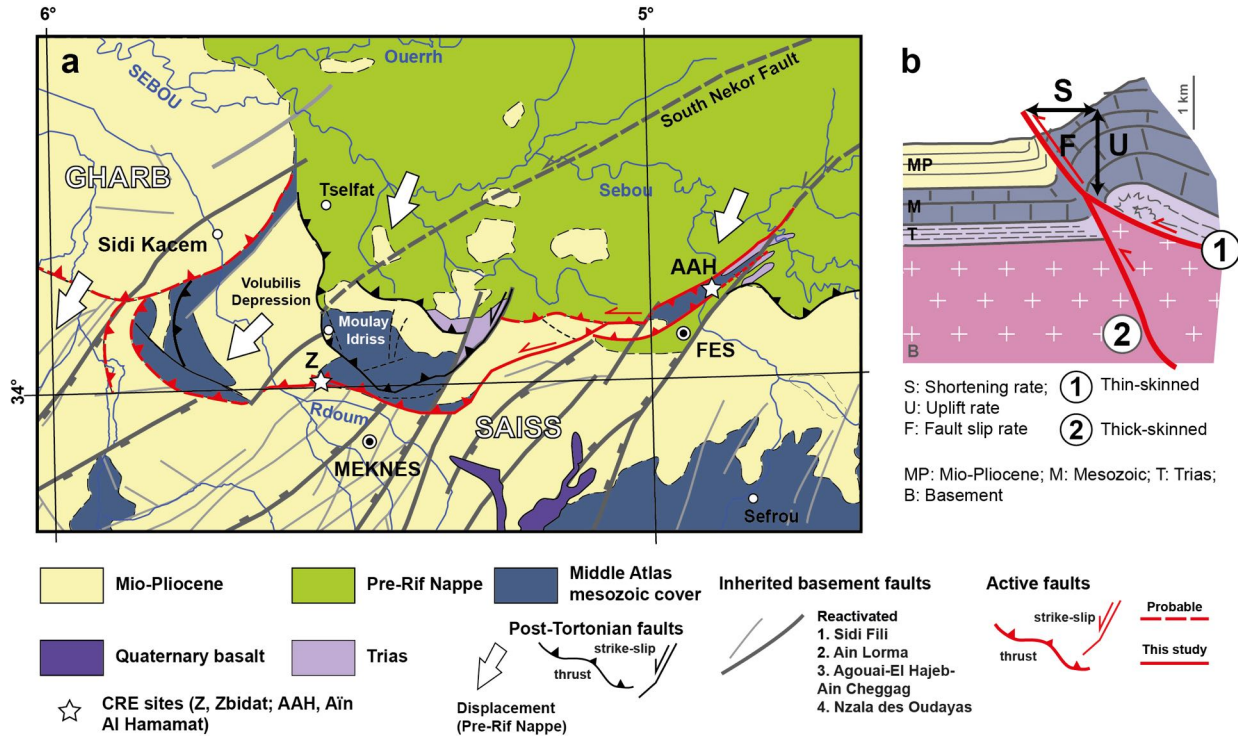
539 non-steady eroding horizon (Lal, 1991). For the six carbonated sandstones, the measured $^{26}\text{Al}/^{10}\text{Be}$
540 ratios range from 3.8 ± 0.3 to 5.9 ± 0.5 , *i.e.*, close to or lower than the theoretical surface steady-state
541 value of 6.1 ± 0.5 (Stone, 2000). The low $^{26}\text{Al}/^{10}\text{Be}$ ratios can be interpreted as reflecting temporary
542 burial of the material (Granger & Muzikar, 2001) or regolith mixing in a slowly eroding landscape
543 (Makhubela et al., 2019).

544 For the carbonate samples, the dispersion of minimum ^{36}Cl exposure suggests that (1) the older
545 samples might also carry cosmogenic content inherited from pre-exposure in the upstream areas,
546 and (2) natural post-abandonment processes (*i.e.*, water runoff, surface deflation) might have,
547 combined with human activities, resulted in upward displacement of cobbles that were initially
548 buried within the first half-metre of alluvial material. This later case could explain the younger
549 ages in the distributions. An alternative interpretation is to consider that the age dispersion is
550 actually representative of the time span of surface activity before abandonment and consequent to
551 an incision of the drainage network. (*e.g.*, Owen et al., 2011). In this scenario, the average value
552 of the age population would fall during the true time span of surface deposition, with the maximum
553 and the minimum ages approximating the beginning of surface activity and the timing of surface
554 abandonment, respectively (D'Arcy et al., 2019).

555 In Zbidat, the central value of 29.6 ± 5.8 ka is only a rough estimate of the abandonment period of
556 the surface. Assuming that the surface abandonment coincided with an abrupt landscape uplift due
557 to the fault activity, the probabilistic approach developed by D'Arcy et al. (2019) considers that
558 this event should be recorded by the age of the youngest sample, depending on the overall period
559 of surface activity. Assuming that the older carbonate cobble is an outlier carrying cosmogenic
560 inheritance, the dispersion of the remaining minimum exposure ages can thus be interpreted as the
561 result of a 41 kyr time-span of surface activity, with a 50% chance of an abandonment time falling
562 between 11 and 22 ka (Fig. 6). In this scenario, the period of surface activity can thus be bracketed
563 between the older peak at 47.7 ± 3.5 ka and the younger peak at 21.4 ± 2.0 ka (Table 4). At Aïn Al
564 Hamamat, considering the older age as an outlier due to cosmogenic inheritance, the lower surface
565 (T_1) may have experienced a 31 kyr time-span of surface activity, with a 63% chance of an
566 abandonment time falling between 11 and 22 kyr (Fig. 7). In this scenario, the lower terrace at Aïn
567 Al Hamamat can be regarded as contemporaneous with the alluvial surface that skirts the piemont
568 of Jbel Zerhoun along the Meknès Section. As for the middle surface (T_2), it may have experienced

569 a 35 kyr time-span of surface activity, with a 48% chance of an abandonment time falling between
 570 25 and 35 kyr (Fig. 7).

571



572

573

574 **Figure 8.** (a) Structural framework showing the relationship between inherited basement normal faults
 575 (after the Carte Néotectonique du Maroc, 1994) and surface expression of active faults along the front of
 576 the Pre-Rif Nappe; (b) Sketch of the main frontal thrust, showing the two rooting possibilities at depth: (1)
 577 a thin-skinned option where the reverse fault sole at about 3-5 km-depth in the Trias, dipping at 30°; (2)
 578 a thick-skinned option where the reverse fault connects to inherited basement faults, dipping at 60°. Arrows
 579 indicate uplift rate (U, 0.6-2.0 mm/yr), estimated from measured incision values and cosmogenic surface
 580 dating, fault slip rate (F, 0.7-4.0 mm/yr) and shortening rate (S, 0.4-3.5 mm/yr), estimated using a fault dip
 581 ranging from 30 to 60°.

582

583 5.2 Estimation of Pleistocene rates of displacement

584 At Zbidat, the 38 m-high topographic escarpment represents the vertical cumulative displacement
 585 generated by a 18 km-long reverse fault segment (Fig. 5). Along the trace of this segment,
 586 temporary streams have cut through the topography, creating 14 m-deep upstream incisions
 587 (Fig. 6). Since there is no temporal constraint on the age of the surface laying at the toe of the
 588 escarpment, the height of the escarpment should be regarded as a minimum value for the vertical
 589 displacement. Assuming that uplift started as early as the onset of surface activity (*i.e.*,

590 47.7±3.5 ka), a minimum vertical rate of 0.8±0.1 mm/yr can be estimated. This assumption is
591 consistent with that of considering an abandonment of the alluvial surface (*i.e.*, 21.4±2.0 ka),
592 which coincides with the onset of the stream incision and yields an incision rate of 0.7±0.1 mm/yr.
593 However, given the uncertainties associated with the dating of the surface abandonment, a wider
594 bracketing of the incision rate between 0.6 and 2.0 mm/yr cannot be ruled out.

595 At Aïn Al Hamamat, the profiles of the stepped terraces exhibit a convincing warping where the
596 Sebou River crosses the front of the Pre-Rif Nappe (Fig. 7). At the latitude of the Jbel Zalagh
597 pressure ridge, the lower, middle and higher terraces lie at elevations of 20±2, 50±2 and 70±2 m-
598 high above the present-day river bed (Fig. 7). In the same area, the Sebou River is also more
599 entrenched into its major flood plain, with an incision of about 7±2 m (Fig. 7). On the one hand,
600 based on the abandonment of the lower and middle terraces at 22.1±4.7 and 29.9±3.2 ka, the
601 topographic positions of these two features above the present-day river bed imply vertical incision
602 rates of the Sebou River of the order of 1.0±0.3 and 1.7±0.2 mm/yr. On the other hand, accounting
603 for the entire periods of surface activity, estimated by the central values of 38.6±3.1 ka (T1) and
604 48.3±2.7 ka (T2), yields lower vertical rates of 0.5±0.1 and 1.0±0.1 mm/yr, respectively. Standing
605 at about 7±2 m above the Sebou River, the major flood plain (T0) is not dated but it is certainly
606 younger than the lower terrace. Assuming a Holocene (11±1 ka) onset for this late river incision
607 yields a rate of about 0.7±0.3 mm/yr, which is consistent with previous lower bound estimates.
608 Since the Sebou River is a major regional drainage system, and without trying to account for
609 transient changes in the watershed during the uplift, one can thus consider that a mean incision
610 rate of 0.9±0.2 mm/yr is a reasonable proxy for the last 50 ka. This value is comparable to the
611 lower bound estimated at Zbidat along the Meknès Section (0.7±0.1 mm/yr). However, if one
612 agrees that tectonic uplift is fully responsible for the stepped geometry of the alluvial terraces along
613 the Sebou River, the roughly 30 m-elevation difference between T1 and T2 should have occurred
614 after the onset of activity of T2 (48.3±2.7 ka) and before that of T1 (38.6±3.1 ka), implying a
615 vertical uplift rate higher than 2 mm/yr over a short time span. Finally, due to the relatively large
616 uncertainties associated with individual samples and the resulting distributed age populations, it is
617 rather speculative to go further on this. In the following, we will thus consider that a value
618 comprised between 0.6 and 2 mm/yr is a conservative proxy for uplift rates associated with the
619 tectonic activity of the faults running along the Pre-Rif Ridges.

620

621

622

623

624

625 Table 5. Seismic hazard parameters from empirical earthquake scaling laws from Thingbaijam et al. (2017) and Hanks and Kanamori
626 (1979). Return times are estimated using a fault slip rate ranging from 0.7 and 4.0 mm/yr.

Segment name	Label of Fig. 5	Sens of motion	Length (km)	Rupture area (km ²) 30° or 60°	Mw	Average displacement (m)	Return time (yr)
Zbidat	L ₁	Reverse	18	254	6.5 ± 0.1	0.6	150-850
Zerhoun	L ₂	Reverse	17	240	6.4 ± 0.1	0.5	140-790
Kennoufa	L ₃	Reverse	19	268	6.5 ± 0.1	0.6	160-920
El Merga	L ₄	Left-lateral	22	311-339	6.3 ± 0.1	0.3	90-500
Tratt	L ₅	Reverse	24	339	6.6 ± 0.1	0.9	220-1290
Meknès	L ₂ +L ₃	Reverse	35	-	6.7 ± 0.1	-	-
Fès	L ₄ +L ₅	Reverse/LL	46	-	7.8 ± 0.2	-	-
All		Reverse	82	-	7.1 ± 0.1	-	-

627

628

629 In the Rif region, geological markers such as the post-nappe surface (Late Tortonian, 7.3 Ma) and
630 the summit surface of the Pre-Rif Nappe (Messinian, 5.3 Ma, to Pliocene, 2.6 Ma) are classically
631 used to gauge long term neotectonics (Morel, 1988, 1989; Carte Néotectonique du Maroc, 1994).
632 Along the deformation front running at the border of the Saïss Basin, these markers exhibit vertical
633 steps ranging from 1600 to 1800 m (Carte Néotectonique du Maroc, 1994), implying long-term,
634 vertical rates of the order of 0.5 ± 0.2 mm/yr. The lower bound of our Pleistocene rate is thus
635 consistent with this integration over the last several millions of years.

636 At the toe of Jbel Tratt in the middle of the Fès Section (Fig. 5), Poujol et al. (2017) described a
637 minimum 12 ± 1 m-high, vertical displacement for an alluvial surface with an optically-stimulated
638 luminescence age ranging from 5.2 ± 0.2 ka (minimum burial age) to 8.1 ± 0.9 ka (central age
639 model). This local observation implies an uplift rate comprised between 1.5 ± 0.3 and
640 2.3 ± 0.3 mm/yr, which is also consistent with the upper bound of our Pleistocene rate estimate.

641 5.3 Seismic hazard parameters

642 In terms of seismogenic potential, the rooting of the Pre-Rif faults at depth is an important
643 parameter to consider. According to published regional cross-sections, the southern deformation
644 front of the external Rif domain could either sole in the Trias at the base of the Mesozoic cover
645 above the African basement at about 3-5 km-depth (Michard et al., 2002; 2008) or into the African
646 lower crust at about 25 km-depth (Frizon de Lamotte et al., 2004). Existing seismic lines along the
647 Fès and Meknès sections, as well as in the external Pre-Rif Ridges (Zizi, 1996; Sani et al., 2007),
648 also favour a rooting in the basement of the Miocene thrusts, reactivating former Mesozoic normal
649 faults (thick-skinned option 2, Fig. 8) rather than within the Trias at about 3-5 km-depth (thin-
650 skinned option 1, Fig. 8). This is also consistent with a focal depth of about 10 km for the 1971
651 Mw 4.6 earthquake, close to Moulay Yacoub (Medina & Cherkaoui, 1992), which could be
652 associated with either the Nzala des Oudayas basement fault or the Pre-Rif front (Fig. 3).

653 On the seismic lines interpreted by Sani et al. (2007), the faults associated with the post-Tortonian
654 uplift of the Pre-Rif Ridges appear relatively steep and rooted in the basement (Fig. 4b), even if
655 they might be shallower towards the surface in other locations (Fig. 4c and Fig. 6e). For the Pre-
656 Rif Ridges a listric geometry has also been considered at greater depth (Poujol et al., 2017;
657 Chalouan et al., 2001). Without additional geometrical constraints, we can assume that the Pre-Rif
658 thrusts are characterized by fault planes dipping between 30° and 60° at depth. Along the Meknès

659 and the Fès sections, the length of the segments are of the order of 17 to 24 km (Fig. 5). According
660 to scaling relationships (*e.g.*, Wells and Coppersmith, 1994; Thingbaijam et al., 2017), this range
661 of surface lengths for reverse faults generally correspond to maximum moment magnitudes of
662 about 6.4-6.8 (Table 5). These magnitude estimates are compatible with intensities ranging
663 between VII and VIII for moderate to large historical earthquakes reported for this region since
664 the eleventh century, and particularly with that of the 1755 *Fès-Meknès Earthquake* (Roux, 1934;
665 El Mrabet, 2005; Paláez et al. 2007; Blanc, 2009; Mourabit et al., 2014; Cherkaoui et al., 2017).
666 Since scaling laws are statistically consistent with self-similarity (*e.g.*, Thingbaijam et al., 2017),
667 relationships between rupture area *vs.* M_w , and rupture length *vs.* M_w offer the opportunity to
668 explore the characteristic seismogenic depth beneath the Pre-Rif Ridges (Table 5). To be
669 consistent with fault dipping between 30° and 60° at depth (Fig. 8), and with the moment
670 magnitudes deduced from segment lengths, the seismogenic depth of the faults should be of the
671 order of 7-12 km (Table 5).

672 Finally, combining measured segment lengths, with estimated seismogenic depths and M_w from
673 scaling relationships on the basis of formulations by Aki (1966) and Hanks & Kanamori (1979)
674 yields average coseismic displacements of the order of 0.4 to 0.9 m (Table 5).

675 Our projection of an uplift rate of 0.6 to 2.0 mm/yr onto a 30 to 60° -dipping fault plane (Fig. 8),
676 would result in conversions to fault slip rates ranging from 0.7 to 4 mm/yr, and shortening rates of
677 0.4 to 3.5 mm/yr (Fig. 8). Even if the fault slip rate is clouded by large uncertainties, such
678 coseismic displacements imply recurrence intervals on the order of a several centuries (Table 5),
679 in good agreement with the historical catalog that describes several $M \approx 6$ events since 1045 CE (El
680 Mrabet, 2005). The bracketing of horizontal shortening is also consistent with that derived by
681 Poujol et al. (2017) and with what is expected from the horizontal GPS velocities and fault block
682 models (*e.g.*, Fadil et al., 2006; Vernant et al., 2010; Koulali et al., 2011). This consistency between
683 the geodetic and geomorphic time scales strongly confirms that the southern border of the Pre-Rif
684 is an important tectonic boundary (*e.g.*, Vernant et al., 2010; Poujol et al., 2017) that probably
685 accommodated most of the shortening associated with the lateral extrusion of the Rif during the
686 Pleistocene.

687 **6 Conclusions**

688 In this study, we revised the regional geomorphic characteristics of the faults running along the
689 front of the Pre-Rif Ridges that constitute the southern border of the Alpine Rif domain in
690 Morocco. Along the ≈ 80 km-long left-lateral, transpressive and reverse fault zone, we provide new
691 geomorphic lines of evidence supporting the Quaternary activity on fault segments that are
692 characterized by lengths of about 20 km. The fault zone can be divided into the Meknès and the
693 Fès sections, which are most probably limited at depth by reactivated, NE-trending basement faults
694 that delineate paleo-grabens associated with the Late Triassic-Jurassic opening of the Atlantic
695 Ocean.

696 Although the chronological dataset provided by cosmogenic nuclides is not straightforward to
697 interpret, the morphochronological approach applied to date stepped alluvial surfaces above the
698 present-day drainage network, allows estimation of incision rates in the range of 0.6-2.0 mm/yr,
699 which can be interpreted as a reasonable proxy for the uplift rate associated with the front of the
700 Pre-Rif Nappe during the last 50 ka.

701 Given their characteristic lengths of about 20 km, the identified fault segments should root in the
702 basement at about 7-12 km-depth, and would have the capacity to generate earthquakes with
703 moment magnitudes of 6.3 to 6.8, average displacements of a few tens of centimetres, and return
704 periods of the order of several hundreds of years. A comparison of different time scales suggests
705 that the fault slip rate associated with the front of the Pre-Rif Nappe has been relatively constant
706 over the last few millions of years, even if a degree of recent acceleration cannot be excluded.
707 Altogether, the results presented in this study imply that the front of the Pre-Rif Nappe is an
708 important structural boundary that may have accommodated most of the Rif lateral extrusion
709 between the Nubia and Iberia tectonic plates.

710 **Acknowledgments**

711 During the revision process, Didier Bourlès sadly passed away. Didier was a renowned scientist
712 who contributed significantly to the development of the technique of cosmogenic nuclides,
713 rendering it essential to many applications in geosciences. We would like to dedicate this article
714 to his memory. This work has been funded by the RiskMED project, Labex OT-Med (ANR-11-
715 LABE-0061) supported by the Investissements d'Avenir, French Government project of the

716 French Agence National pour la Recherche (ANR) through the A*MIDEX project (ANR-1-1E-
 717 0001-02). The Pléiades images used in this study were specifically acquired through an ISIS
 718 Project funded by the CNES (FC-193978-2018-311-U.AIX-Marseille CEREGE). The ASTER
 719 AMS national facility (CEREGE, Aix-en-Provence), where the ^{10}Be , ^{26}Al , and ^{36}Cl measurements
 720 were carried out, is supported by the INSU/CNRS, the ANR through the Projets thématiques
 721 d'excellence programme for the Equipements d'Excellence ASTER-CEREGE action, and the
 722 IRD. We thank Georges Aumaître and Karim Keddadouche for their continuing expertise in
 723 Accelerator Mass Spectrometry measurements. Datasets for this research are available in this in-
 724 text data citation references: Agharroud et al. (2021) [Creative Commons Attribution 4.0
 725 International]. The AW3D30 (version 3.1) topographic data used for this paper is provided by the
 726 Japan Aerospace Exploration Agency. We thank Régis Braucher and Lucilla Benedetti, from
 727 CEREGE, as well as Philippe Vernant, from Montpellier University, and Jason Williams, from
 728 Leeds University, for thoughtful reviews of an early version of this paper. We thank both Timothy
 729 Byrne, from University of Connecticut, and Edward Anthony, from Aix-Marseille University, for
 730 editing the English. Figure 1 was created using the GMT software package. Taylor Schildgen and
 731 Duna Roda-Boluda are thanked for their editorial handling of the manuscript.

732 **References**

- 733 Abbassi, A., Cipollari, P., Zaghloul, M.N., Cosentino, D. (2020). The Rif Chain (Northern Morocco) in
 734 the Late Tortonian-Early Messinian Tectonics of the Western Mediterranean orogenic belt: Evidence
 735 from the Tanger-Al Manzla wedge-top Basin. *Tectonics*, 39(9), e2020TC006164.
- 736 Agharroud, K., Siame, L., Ben Moussa, A., Bellier, O., Guillou, V., Fleury, J., El Kharim, Y. (2021).
 737 AMS results for cosmogenic exposure dating along the Southern Rif Front of Morocco (Version 1.0)
 738 [Data set]. Zenodo. <http://doi.org/10.5281/zenodo.4543677>.
- 739 Aki, K. (1966). Generation and Propagation of G Waves from the Niigata Earthquake of June 16, 1964:
 740 Part 1. A statistical analysis. 東京大學地震研究所彙報= Bulletin of the Earthquake Research
 741 Institute, University of Tokyo, 44(1), 23-72.
- 742 Ansberque, C., Bellier, O., Godard, V., Lasserre, C., Wang, M., Braucher, R., Talon, B., de Sigoyer, J.,
 743 Xu, X., Bourlès, D. L. (2016). The Longriqu fault zone, eastern Tibetan Plateau: segmentation and
 744 Holocene behavior. *Tectonics*, 35(3), 565-585.
- 745 Arnold, M., Merchel, S., Bourlès, D. L., Braucher, R., Benedetti, L., Finkel, R. C., Aumaître, G.,
 746 Gott dang, A., Klein, M. (2010). The French accelerator mass spectrometry facility ASTER: improved
 747 performance and developments. *Nuclear Instruments and Methods in Physics Research Section B:
 748 Beam Interactions with Materials and Atoms*, 268(11-12), 1954-1959.

- 749 Baratin, L. M., Mazzotti, S., Chéry, J., Vernant, P., Tahayt, A., Mourabit, T. (2016). Incipient mantle
750 delamination, active tectonics and crustal thickening in Northern Morocco: Insights from gravity data
751 and numerical modeling. *Earth and Planetary Science Letters*, 454, 113-120.
- 752 Bargach, K., Ruano, P., Chabli, A., Galindo-Zaldívar, J., Chalouan, A., Jabaloy, A., Akil, M., Ahmamou,
753 M., Sanzde Galdeano, C., Benmakhlof, M. (2004). Recent tectonic deformations and stresses in the
754 frontal part of the Rif Cordillera and the Saïss Basin (Fes and Rabat regions, Morocco). *Pure and*
755 *Applied Geophysics*, 161(3), 521-540.
- 756 Bendkik, A., Chenakeb, M., El Youssfi, H., Kerzazi, K., Valleri, G., Lamdaouar, K. (2004). Carte
757 géologique du Maroc, Sidi Kacem, échelle 1:50000. Service géologique du Maroc, Notes et mémoires.
- 758 Bernard, M., Decluseau, D., Gabet, L., Nonin, P. (2012). 3D capabilities of Pleiades satellite.
759 International archives of the photogrammetry. Remote Sensing and Spatial Information Sciences, 39,
760 553–557. doi: 10.5194/isprsarchives-XXXIX-B3-553-201
- 761 Bezada, M. J., Humphreys, E. D., Toomey, D. R., Harnafi, M., Dávila, J. M., Gallart, J. (2013). Evidence
762 for slab rollback in westernmost Mediterranean from improved upper mantle imaging. *Earth Planet.*
763 *Sci. Lett.*, 368, 51-60.
- 764 Blanc, P.-L. (2009). Earthquakes and tsunami in november 1755 in morocco: a different reading of
765 contemporaneous documentary sources. *Natural Hazards & Earth System Sciences*, 9(3). doi:
766 10.5194/nhess-9-725-2009
- 767 Borchers, B., Marrero, S., Balco, G., Caffee, M., Goehring, B., Lifton, N., Nishiizumi, K., Philips, F.,
768 Schaefer, J., Stone, J. (2016). Geological calibration of spallation production rates in the CRONUS-
769 Earth project. *Quaternary Geochronology*, 31, 188–198. doi: 10.1016/j.quageo.2015.01.009
- 770 Braucher, R., Del Castillo, P., Siame, L., Hidy, A. J., Bourlès, D. L. (2009). Determination of both
771 exposure time and denudation rate from an in situ-produced ^{10}Be depth profile: a mathematical proof
772 of uniqueness. Model sensitivity and applications to natural cases. *Quaternary Geochronology*, 4(1),
773 56-67.
- 774 Braucher, R., Guillou, V., Bourlès, D.L., Arnold, M., Aumaître, G., Keddadouche K., & Nottoli, E.,
775 (2015). Preparation of ASTER in-house $^{10}\text{Be}/^{9}\text{Be}$ standard solutions. *Nuclear Instruments and*
776 *Methods in Physics Research B*, 361, 354-360.
- 777 Braucher, R., Merchel, S., Borgomano, J., Bourlès, D. (2011). Production of cosmogenic radionuclides at
778 great depth: A multi element approach. *Earth and Planetary Science Letters*, 309(1-2), 1–9. doi:
779 10.1016/j.epsl.2011.06.036
- 780 Braucher, R., Keddadouche, K., Aumaître, G., Bourlès, D.L., Arnold, M., Pivot, S. (2018). *Nuclear Inst.*
781 *and Methods in Physics Research B* Chlorine measurements at the 5MV French AMS national facility
782 ASTER : Associated external uncertainties and comparabil- ity with the 6MV DREAMS facility.
783 *Nuclear Inst. and Methods in Physics Research, B*, 420(January), 40–45. doi:
784 10.1016/j.nimb.2018.01.025
- 785 Brown, E. T., Edmond, J. M., Raisbeck, G. M., Yiou, F., Kurz, M. D., Brook, E. J. (1991). Examination
786 of surface exposure ages of Antarctic moraines using in situ produced ^{10}Be and ^{26}Al . *Geochimica et*
787 *Cosmochimica Acta*, 55(8), 2269–2283. doi: 10.1016/ 0016-7037(91)90103-C

- 788 Carte Néotectonique du Maroc, Echelle 1/1000000, Feuille 1: Provinces du Nord. Royaume du Maroc,
789 Ministère de l'Énergie et des Mines, Direction de la Géologie, Editions du Service Géologique du
790 Maroc, 1994.
- 791 Chalouan, A., Gil, A. J., Galindo-Zaldívar, J., Ahmamou, M., Ruano, P., de Lacy, M. C., Ruiz-
792 Armenteros, A. M., Benmakhlouf, M., Riguzzi, F. (2014). Active faulting in the frontal Rif Cordillera
793 (Fez region, Morocco): constraints from GPS data. *Journal of Geodynamics*, 77 (Geodynamic
794 evolution of the Alboran domain), 110–122. doi: 10.1016/j.jog.2014.01.002
- 795 Chalouan, A., Michard, A., El Kadiri, K., Negro, F., De Lamotte, D. F., Soto, J. I., Saddiqi, O. (2008).
796 The Rif Belt. In *Continental evolution: the geology of Morocco* (pp. 203-302). Springer, Berlin,
797 Heidelberg.
- 798 Chalouan, A., Michard, A., Feinberg, H., Montigny, R., Saddiqi, O. (2001). The rif mountain building
799 (morocco); a new tectonic scenario. *Bulletin de la Société géologique de France*, 172(5), 603–616. doi:
800 10.2113/172.5.603
- 801 Chenakeb, M., Bendkik, A., Zouibaa A. (2004). Carte géologique du Maroc, Beni Ammar, échelle
802 1:50000. Service géologique du Maroc, Notes et mémoires. ISSN : 03691748.
- 803 Cherkaoui, T. (1991). Contribution à l'étude de l'aléa sismique au maroc : le séisme d'Agadir
804 (29/02/1960) et la microsismicité d'Al Hoceima (PhD, Université de Grenoble). Grenoble.
- 805 Cherkaoui, T., Asebriy, L. (2003). Le risque sismique dans le Nord du Maroc. *Travaux de l'Institut*
806 *Scientifique, Série Géologie et Géographie physique*, 21, 225–232.
- 807 Cherkaoui, T., Medina, F. (1988). Révision des données macrosismiques et du mécanisme au foyer du
808 séisme d' Agadir du 29 février 1960 . *Revue de géographie du Maroc*, 12, 51–61.
- 809 Cherkaoui, T., Medina, F., Mridekh, A. (2017). Re-examination of the historical 11 May, 1624 Fez
810 earthquake parameters. *Física de la Tierra*, 29, 135–157. doi: 10.5209/FITE.57469
- 811 Chmeleff, J., von Blanckenburg, F., Kossert, K., Jakob, D. (2010). Determination of the ^{10}Be half-life by
812 multicollector ICP-MS and liquid scintillation counting. *Nuclear Instruments and Methods in Physics*
813 *Research, Section B: Beam Interactions with Materials and Atoms*, 268(2), 192–199. doi:
814 10.1016/j.nimb.2009.09.012
- 815 Choubert, G., Faure-Muret, A. (1962). Evolution du domaine atlasique marocain depuis les temps
816 paléozoïques. *Livre Mém Fallot Mém Geol Fr*, 1, 447-527
- 817 D'Arcy, M., Schildgen, T., Turowski, J., DiNezio, P. (2019). Inferring the timing of abandonment of
818 aggraded alluvial surfaces dated with cosmogenic nuclides. *Earth Surface Dynamics*, 7, 755-771.
- 819 De Reu, J., Bourgeois, J., Bats, M., Zwertvaegher, A., Gelorini, V., De Smedt, P., Chu, W., Antrop, M.,
820 De Maeyer, P., Finke, P., Van Meirvenne, M., Verniers, J., Crombé, P (2013). Application of the
821 topographic position index to heterogeneous landscapes. *Geomorphology*, 186, 39-49.
- 822 De Vicente, G. D., Cloetingh, S. A. P. L., Muñoz-Martín, A., Olaiz, A., Stich, D., Vegas, R., Galindo-
823 Zaldívar, J., Fernández-Lozano, J. (2008). Inversion of moment tensor focal mechanisms for active
824 stresses around the microcontinent Iberia: Tectonic implications. *Tectonics*, 27(1).

- 825 Delunel, R., Beek, P. A., Bourlès, D. L., Carcaillet, J., Schlunegger, F. (2014), Transient sediment supply
 826 in a high-altitude Alpine environment evidenced through a ¹⁰Be budget of the Etages catchment
 827 (French Western Alps), *Earth Surf. Processes Landforms*, 39(7), 890–899.
- 828 Dunai, T. (2010). *Cosmogenic nuclides : principles, concepts and applications in the earth surface*
 829 *sciences*. Cambridge University Press.
- 830 Dziewonski, A. M., Chou, T. A., Woodhouse, J.H. (1981), Determination of earthquake source
 831 parameters from waveform data for studies of global and regional seismicity. *J. Geophys. Res.* 86,
 832 2825-2852. doi:10.1029/JB086iB04p02825
- 833 Ekström, G., Nettles, M., Dziewonski, A. M. (2012), The global CMT project 2004-2010: Centroid-
 834 moment tensors for 13,017 earthquakes. *Phys. Earth Planet. Inter.* 200-201, 1-9.
 835 doi:10.1016/j.pepi.2012.04.002
- 836 El Alami, O., Medina, F., Jebli, F. (1992). Etude du séisme d'Agadir du 5 avril 1992. GAIA- Ecological
 837 Perspectives on Science and Society, 5, 1–5.
- 838 El Alami, O., Tadili, B.A., Cherkaoui, T.E., Médina, F., Ramdani, M., Aït Brahim, L., Harnafi, M.
 839 (1998). The Al Hoceima earthquake of May 26, 1994 and its aftershocks: a seismotectonic study.
 840 *Annali di geofisica*, 41, 519–537. doi: 10.4401/ag-3801
- 841 El Mrabet, T. A. (2005). *The Great Earthquakes in the Maghreb region and their consequences on man*
 842 *and environment (CNRST-LAG ed.)*. Rabat, Morocco.
- 843 Etheve, N., Frizon de Lamotte D., Mohn G., Martos, R., Roca E., Blanpied, C. (2016). Extensional vs
 844 contractional Cenozoic deformation in Ibiza (Balearic Promontory, Spain): Integration in the West
 845 Mediterranean back-arc setting. *Tectonophysics*, 682, 35–55.
- 846 Faccenna, C., Piromallo, C., Crespo-Blanc, A., Jolivet, L., Rossetti, F., 2004. Lateral slab deformation
 847 and the origin of the western Mediterranean arcs. *Tectonics* 23, TC1012.
- 848 Fadil, A., Vernant, P., McClusky, S., Reilinger, R., Gomez, F., Sari, D. B., Mourabit, T., Feigl, K.,
 849 Barazangi, M. (2006). Active tectonics of the western Mediterranean: Geodetic evidence for rollback
 850 of a delaminated subcontinental lithospheric slab beneath the Rif Mountains,
 851 Morocco. *Geology*, 34(7), 529-532.
- 852 Faugères, J.C. (1978). *Les rides sud-rifaines : Evolution sédimentaire et structurale d'un bassin atlantico-*
 853 *mésogéen de la marge africaine [unpublished Ph. D. Thesis]*, Université de Bordeaux I, Bordeaux.
- 854 Frizon de Lamotte, D., Crespo-Blanc, A., Saint-Bézar, B., Comas, M., Fernandez, M., Zeyen, H., Ayarza,
 855 P., Robert-Charue, C., Chalouan, A., Zizi, M., Teixell, A., Arboleya, M.-L., Alvarez-Lobato, F.,
 856 Julivert, M., Michard, A. (2004). TRANSMED Transect I: Iberian Meseta–Guadalquivir Basin–Betic
 857 Cordillera–Alboran Sea–Rif–Moroccan Meseta–High Atlas–Sahara Platform, *in Cavazza, W., &*
 858 *Stampfli, G. M., The TRANSMED Atlas: The Mediterranean Region from Crust to Mantle*, Springer,
 859 Berlin, 141 p.
- 860 Fukao, (1973). Thrust faulting at a lithospheric plate boundary, the Portugal earthquake of 1969, *Earth*
 861 *and Planetary Science Letters*. 18, 205-216.
- 862 Galbis Rodriguez, J. (1932). *Catalogo sismico de la zona comprendida entre los meridianos 5°E y 20°W*
 863 *de Greenwich y los paralelos 45° y 25°N, I (Instituto geográfico y catastral ed.)*. Galbis Rodriguez, J.

- 864 (1940). Catalogo sismico de la zona comprendida entre los meridianos 5°E y 20°W de Greenwich y los
865 paralelos 45° y 25°N, II (Instituto geográfico y catastral ed.).
- 866 Galbis Rodriguez, J. (1940). Catalogo sismico de la zona comprendida entre los meridianos 5°E y 20°W
867 de Greenwich y los paralelos 45° y 25°N. II, Instituto geográfico y catastral, 207 p.
- 868 Galbraith, R. F., Green, P. F. (1990). Estimating the component ages in a finite mixture. *International*
869 *Journal of Radiation Applications and Instrumentation. Part D. Tracks and Radiation Measurements*,
870 17(3), 197–206. doi: 10.1016/1359-0189(90)90035-V.
- 871 Giaconia, F., Booth-Rea, G., Martínez-Martínez, J. M., Azañón, J. M., Pérez-Peña, J. V., Pérez-Romero,
872 J., Villegas, I. (2012). Geomorphic evidence of active tectonics in the Sierra Alhamilla (eastern Betics,
873 SE Spain). *Geomorphology*, 145, 90-106.
- 874 Gimeno-Vives, O., de Lamotte, D. F., Leprêtre, R., Haissen, F., Atouabat, A., Mohn, G. (2020). The
875 structure of the Central-Eastern External Rif (Morocco); Poly-phased deformation and role of the
876 under-thrusting of the North-West African paleo-margin. *Earth-Science Reviews*, 103198.
- 877 Gosse, J. C., Phillips, F. M. (2001). Terrestrial in situ cosmogenic nuclides: theory and application.
878 *Quaternary Science Reviews*, 20, 1475-1560.
- 879 Granger, D. E., Muzikar, P. F. (2001). Dating sediment burial with in situ-produced cosmogenic nuclides:
880 theory, techniques, and limitations. *Earth and Planetary Science Letters*, 188(1-2), 269-281.
- 881 Gutscher, M. A. (2004). What caused the great Lisbon earthquake?. *Science*, 305(5688), 1247-1248.
- 882 Gutscher, M. A., Baptista, M. A., Miranda, J. M. (2006). The Gibraltar Arc seismogenic zone (part 2):
883 constraints on a shallow east dipping fault plane source for the 1755 Lisbon earthquake provided by
884 tsunami modeling and seismic intensity. *Tectonophysics*, 426(1-2), 153-166.
- 885 Hanks, T. C., Kanamori, H. (1979). A moment magnitude scale. *Journal of Geophysical Research: Solid*
886 *Earth*, 84(B5), 2348–2350. doi: 10.1029/JB084iB05p02348
- 887 Hatzfeld, D., Frogneux, M. (1981). Intermediate depth seismicity in the western Mediterranean unrelated
888 to subduction of oceanic lithosphere (Vol. 292) (No. 5822). doi: 10.1038/292443a0
- 889 International Seismological Centre (2020), On-line Bulletin, On-line
890 Bulletin, <https://doi.org/10.31905/D808B830>.
- 891 Johnston, A. C. (1996). Seismic moment assessment of earthquakes in stable continental regions—III.
892 New Madrid 1811–1812, Charleston 1886 and Lisbon 1755. *Geophysical Journal*
893 *International*, 126(2), 314-344.
- 894 Jomard, H., Cushing, E. M., Palumbo, L., Baize, S., David, C., & Chartier, T. (2017). Transposing an
895 active fault database into a seismic hazard fault model for nuclear facilities—Part 1: Building a database
896 of potentially active faults (BDFFA) for metropolitan France. *Natural Hazards and Earth System*
897 *Sciences*, 17(9), 1573-1584.
- 898 Korschinek, G., Bergmaier, A., Dillmann, I., Faestermann, T., Gerstmann, U., Knie, K., Lierse von
899 Gostomski, C., Maiti, M., Poutivtsev, M., Remmert, A., Rugel, G., Wallner, Anton (2009).
900 Determination of the ¹⁰Be half-life by hi-ERD and liquid scintillation counting. *Geochimica et*
901 *Cosmochimica Acta Supplement*, 73, A685.

- 902 Koulali, A., Ouazar, D., Tahyat, A., King, R.W., Vernant, P., Reilinger, R.E., McClusky, S., Mourabit, T.,
 903 Davila, J.M. Amraoui, N. (2011), New GPS constraints on active deformation along the Africa-Iberia
 904 Plate Boundary. *Earth Planet. Sci. Lett.* 308, 211–217.
- 905 Lal, D. (1991). Cosmic ray labeling of erosion surfaces: in situ nuclide production. *Earth and Planetary*
 906 *Science Letters*, 104, 424–439. doi: 10.1016/0012-821X(91)90220-C
- 907 Landgraf, A., Kübler, S., Hintersberger, E., Stein, S. (2017). Active tectonics, earthquakes and
 908 palaeoseismicity in slowly deforming continents. *Geological Society, London, Special*
 909 *Publications*, 432(1), 1-12.
- 910 Lindsay, J. B., Cockburn, J. M. H., Russell, H. A. J. (2015). An integral image approach to performing
 911 multi-scale topographic position analysis. *Geomorphology*, 245, 51-61.
- 912 Lindsay, J.B. (2016). Whitebox GAT: A case study in geomorphometric analysis. *Computers &*
 913 *Geosciences*, 95, 75-84. DOI: 10.1016/j.cageo.2016.07.003
- 914 Makhubela, T. V., Kramers, J. D., Scherler, D., Wittmann, H., Dirks, P. H. G. M., Winkler, S. R. (2019).
 915 Effects of long soil surface residence times on apparent cosmogenic nuclide denudation rates and
 916 burial ages in the Cradle of Humankind, South Africa. *Earth Surface Processes and*
 917 *Landforms*, 44(15), 2968-2981.
- 918 Martinez-Solares, J. M., Arroyo, A. L., Mezcuca, J. (1979). Isoseismal map of the 1755 Lisbon earthquake
 919 obtained from Spanish data. *Tectonophysics*, 53(3-4), 301-313.
- 920 Matias, L. M., Cunha, T., Annunziato, A., Baptista, M. A., Carrilho, F. (2013). Tsunamigenic earthquakes
 921 in the Gulf of Cadiz: Fault model and recurrence. *Natural Hazards and Earth System Science*, 13(1),
 922 1–13. doi: 10.5194/nhess-13-1-2013
- 923 McClusky, S., Reilinger, R., Mahmoud, S., Ben Sari, D., Tealeb, A. (2003). GPS constraints on Africa
 924 (Nubia) and Arabia plate motions. *Geophysical Journal International*, 155(1), 126-138.
- 925 Medina, F., Cherkaoui, T. (1992). Mécanismes au foyer des séismes du Maroc et des régions voisines
 926 (1959 – 1986). Conséquences tectoniques. *Eclogae Geologicae Helveticae*, 85/5, 433-457.
- 927 Merchel, S., Bremser, W. (2004). First international ²⁶Al interlaboratory comparison - Part I. In *Nuclear*
 928 *instruments and methods in physics research, section b: Beam interactions with materials and atoms*
 929 (Vol. 223-224, pp. 393–400). doi: 10.1016/j.nimb.2004.04.076
- 930 Merchel, S., Herpers, U. (1999). An update on radiochemical separation techniques for the determination
 931 of long-lived radionuclides via accelerator mass spectrometry. *Radiochimica Acta*, 84(4), 215–220.
- 932 Merchel, S., Arnold, M., Aumaître, G., Benedetti, L., Bourlès, D. L., Braucher, R., Alfimov, V., Freeman,
 933 S. P. H. T., Steier, P., Wallner, A. (2008). Towards more precise ¹⁰Be and ³⁶Cl data from
 934 measurements at the 10⁻¹⁴ level: Influence of sample preparation. *Nuclear Instruments and Methods in*
 935 *Physics Research, Section B: Beam Interactions with Materials and Atoms*, 266(22), 4921–4926.
- 936 Merchel, S., Bremser, W., Alfimov, V., Arnold, M., Aumaître, G., Benedetti, L., Bourlès, D. L., Caffee,
 937 M., Fifield, L. K., Finkel, R. C., Freeman, S. P. H. T., Martschini, M., Matsushi, Y., Rood, D. H.,
 938 Sasa, K., Steier, P., Takahashi, T., Tamari, M., Tims, S. G., Tosaki, Y., Wilcken, K. M., Xu, S. (2011).
 939 Ultra-trace analysis of ³⁶Cl by accelerator mass spectrometry: an interlaboratory study. *Analytical and*
 940 *bioanalytical chemistry*, 400(9), 3125–32. doi: 10.1007/s00216-011-4979-2

- 941 Michard, A., Chalouan, A., Feinberg, H., Goffé, B., Montigny, R. (2002). How does the alpine belt end
 942 between Spain and Morocco? *Bulletin de la Société géologique de France*, 173(1), 3–15. doi:
 943 10.2113/173.1.3
- 944 Michard, A., Saddiqi, O., Chalouan, A., de Lamotte, D. F. (2008). Continental evolution: The geology
 945 of Morocco: Structure, stratigraphy, and tectonics of the Africa-Atlantic-Mediterranean triple junction
 946 (Vol. 116). Springer.
- 947 Moratti, G., Piccardi, L., Vannucci, G., Belardinelli, M. E., Dahmani, M., Bendkik, A., Chenakeb, M.
 948 (2003). The 1755 "Meknes" earthquake (Morocco): Field data and geodynamic implications. *Journal*
 949 *of Geodynamics*, 36(1-2), 305–322.
- 950 Morel, J. L., Meghraoui, M. (1996). Goringe-Alboran-Tell tectonic zone: A transpression system along
 951 the Africa-Eurasia plate boundary. *Geology*, 24(8), 755-758.
- 952 Morel, J.L. (1988). Evolution récente de l'orogène rifain et de son avant pays depuis la fin de la mise en
 953 place des nappes (Rif-Maroc). *Mem Geodiffusion*, 4, 584.
- 954 Morel, J.L. (1989). Etats de contrainte et cinématique de la chaîne rifaine (Maroc) du Tortonien à l'actuel.
 955 *Geodynamica Acta*, 3, 238-294.
- 956 Moreno, B., Atakan, K., Furuløkken, K. A., Temel, S., Berland, O. J. (2004). SAFE-tools: A web-based
 957 application for identification of active faults. *Seismological Research Letters*, 75(2), 205-213.
- 958 Moulin, A., Benedetti, L., Rizza, M., Jamšek Rupnik, P., Gosar, A., Bourlès, D., Keddadouche, K.,
 959 Aumaître, G., Arnold, M., Guillou, V., Ritz, J. F. (2016). The Dinaric fault system: Large-scale
 960 structure, rates of slip, and Plio-Pleistocene evolution of the transpressive northeastern boundary of the
 961 Adria microplate. *Tectonics*, 35(10), 2258-2292.
- 962 Mourabit, T., Abou Elenean, K. M., Ayadi, A., Benouar, D., Ben Suleman, A., Bezzeghoud, M.,
 963 Cheddadi, A., Chourak, M., ElGabry, M. N., Harbi, A., Hfaied, M., Hussein, H.M., Kacem, J., Jabour,
 964 N., Magrin, A., Maouche, S., Meghraoui, M., Ousadou, F., Panza, G. F., Peresan, A., Romdhane, N.,
 965 Vaccari, F., Zuccolo, E. (2014). Neo-deterministic seismic hazard assessment in North Africa. *Journal*
 966 *of Seismology*, 18(2), 301–318. doi: 10.1007/s10950-013-9375-2
- 967 Nishiizumi, K. (2004). Preparation of ²⁶Al AMS standards. In *Nuclear instruments and methods in*
 968 *physics research, section b: Beam interactions with materials and atoms*, 223-224, 388–392. doi:
 969 10.1016/j.nimb.2004.04.075
- 970 Nishiizumi, K., Imamura, M., Caffee, M. W., Southon, J. R., Finkel, R. C., McAninch, J. (2007).
 971 Absolute calibration of ¹⁰Be AMS standards. *Nuclear Instruments and Methods in Physics Research,*
 972 *Section B: Beam Interactions with Materials and Atoms*, 258(2), 403–413. doi:
 973 10.1016/j.nimb.2007.01.297
- 974 Owen, L. A., Frankel, K. L., Knott, J. R., Reynhout, S., Finkel, R. C., Dolan, J. F., Lee, J. (2011).
 975 Beryllium-10 terrestrial cosmogenic nuclide surface exposure dating of Quaternary landforms in Death
 976 Valley. *Geomorphology*, 125(4), 541-557.
- 977 Panagiotakis, E., Chrysoulakis, N., Charalampopoulou, V., Poursanidis, D. (2018). Validation of Pleiades
 978 Tri-Stereo DSM in urban areas. *ISPRS International Journal of Geo-Information*, 7(3), 118.

- 979 Peláez, J.A., Chourak, M., Tadili, B.A., Aït Brahim, L., Hamdache, M., López Casado, C., Martínez
 980 Solares, J. M. (2007). A catalog of main Moroccan earthquakes from 1045 to 2005. *Seismological*
 981 *Research Letters*, 78(6), 614–621. doi: 10.1785/gssrl.78.6.614
- 982 Pereira De Sousa, F. (1919). The 1755, November 1 Earthquake: a demographic study (Geological
 983 Services of Portugal ed.; Tech. Rep.). Portugal.
- 984 Pérouse, E., Vernant, P., Chéry, J., Reilinger, R., McClusky, S. (2010). Active surface deformation and
 985 sub-lithospheric processes in the western Mediterranean constrained by numerical
 986 models. *Geology*, 38(9), 823-826.
- 987 Poujol, A., Ritz, J. F., Tahayt, A., Vernant, P., Condomines, M., Blard, P. H., Billant, J., Vacher, L.,
 988 Tibari, B., Hni, L., Koulali Idrissi, A. (2014). Active tectonics of the Northern Rif (Morocco) from
 989 geomorphic and geochronological data. *Journal of Geodynamics*, 77, 70-88.
- 990 Poujol, A., Ritz, J. F., Vernant, P., Huot, S., Maate, S., Tahayt, A. (2017). Which fault destroyed Fes city
 991 (Morocco) in 1755? A new insight from the Holocene deformations observed along the southern
 992 border of Gibraltar arc. *Tectonophysics*, 712-713, 303–311. doi: 10.1016/j.tecto.2017.05.036
- 993 Ritz, J. F., Baize, S., Ferry, M., Larroque, C., Audin, L., Delouis, B., Mathot, E. (2020). Surface rupture
 994 and shallow fault reactivation during the 2019 Mw 4.9 Le Teil earthquake, France. *Communications*
 995 *Earth & Environment*, 1(1), 1-11.
- 996 Rizza, M., Abdrakhmatov, K., Walker, R., Braucher, R., Guillou, V., Carr, A. S., Campbell, G.,
 997 McKenzie, D., Jackson, J., Aumaître, G., Bourlès, D.L., Keddadouche, K. (2019). Rate of slip from
 998 multiple Quaternary dating methods and paleoseismic investigations along the Talas-Fergana Fault:
 999 Tectonic implications for the Tien Shan Range. *Tectonics*, 38(7), 2477-2505.
- 1000 Roux, G. (1934). Notes sur les tremblements de terre ressentis au Maroc avant 1933. *Mémoire de la*
 1001 *société scientifique nationale du Maroc*, 39, 42–71.
- 1002 Rupnik, E., Pierrot-Deseilligny, M., Delorme, A. (2018). 3D reconstruction from multi-view VHR-
 1003 satellite images in MicMac. *ISPRS Journal of Photogrammetry and Remote Sensing*, 139, 201–211.
 1004 doi: 10.1016/j.isprsjprs.2018.03.016
- 1005 Ryerson, F. J., Tapponnier, P., Finkel, R. C., Meriaux, A.-S., Van der Woerd, J., Lasserre, C., Chevalier,
 1006 M.-L., Xu, X.-M., King, G. C. (2006). Applications of morphochronology to the active tectonics of
 1007 Tibet. *in Siame, L.L., Bourlès, D.L., and Brown, E.T., eds. In Situ-Produced Cosmogenic Nuclides*
 1008 *and Quantification of Geological Processes: Geological Society of America Special Paper 415*, p. 61-
 1009 86, doi: 10.1130/2006.2415(05).
- 1010 Sani, F., Del Ventisette, C., Montanari, D., Bendkik, A., Chenakeb, M. (2007). Structural evolution of the
 1011 Rides Prerifaines (Morocco): structural and seismic interpretation and analogue modelling
 1012 experiments. *International Journal of Earth Sciences*, 96(4), 685-706.
- 1013 Schimmelpfennig, I., Benedetti, L., Finkel, R., Pik, R., Blard, P.-H., Bourlès, D., Burnard, P., Williams,
 1014 A. (2009). Sources of in-situ ³⁶Cl in basaltic rocks. Implications for calibration of production rates.
 1015 *Quaternary Geochronology*, 4(6), 441–461. doi: 10.1016/j.quageo.2009.06.00

- 1016 Sébrier, M., Siame, L., Zouine, E. M., Winter, T., Missenard, Y., Leturmy, P. (2006). Active tectonics in
 1017 the Moroccan High Atlas. *Comptes Rendus - Geoscience*, 338(1-2), 65–79. doi:
 1018 10.1016/j.crte.2005.12.001
- 1019 Siame, L. L., Chen, R. F., Derrieux, F., Lee, J. C., Chang, K. J., Boulès, D. L., Braucher, R., Leanni, L.,
 1020 Kang, C. C., Chang, C. P., Chu, H. T. (2012). Pleistocene alluvial deposits dating along frontal thrust
 1021 of Changhua Fault in western Taiwan: The cosmic ray exposure point of view. *Journal of Asian Earth
 1022 Sciences*, 51, 1-20.
- 1023 Siame, L., Sébrier, M. (2004). Determination of a basic set of diagnostic criteria to identify and
 1024 characterize slow active faults. Deliverable Re9.3 (WP9: Criteria for characterizing slow active faults
 1025 and standardization of paleoseismological analyses) of S.A.F.E. Project (European Project EVG1-
 1026 2000-22005).
 1027 [https://www.researchgate.net/publication/233944555_Siame_LL_and_Sebrier_M_2004_Determinatio
 1028 n_of_a_basic_set_of_diagnostic_criteria_to_identify_and_characterise_slow_active_faults_Deliverab
 1029 le_Re93_Workpackage9_Criteria_for_characterising_slow_active_f](https://www.researchgate.net/publication/233944555_Siame_LL_and_Sebrier_M_2004_Determination_of_a_basic_set_of_diagnostic_criteria_to_identify_and_characterise_slow_active_faults_Deliverable_Re93_Workpackage9_Criteria_for_characterising_slow_active_f)
- 1030 Stone, J. O. (2000). Air pressure and cosmogenic isotope production. *Journal of Geophysical Re- search*,
 1031 105(B10), 23753–23759. doi: 10.1029/2000JB90018
- 1032 Suter, G. (1980). Carte géologique/structurale de la chaîne rifaine, échelle 1:500000. Service des Cartes
 1033 géologiques, Maroc.
- 1034 Takaku, J., Tadono, T., Tsutsui, K., Ichikawa M. (2018). Quality Improvements of 'AW3D' Global DSM
 1035 Derived from ALOS PRISM. *Proc. IGARSS2018, IEEE*, Valencia, Spain, 1612-1615.
- 1036 Takaku, J., Tadono, T., Tsutsui, K., Ichikawa, M. (2014). Validation of 'AW3D' Global DSM Generated
 1037 from ALOS PRISM, *ISPRS Annals of the Photogrammetry, Remote Sensing and Spatial Information
 1038 Sciences*, III-4, 25-31.
- 1039 Thiebot, E., Gutscher, M. A. (2006). The Gibraltar Arc seismogenic zone (part 1): constraints on a
 1040 shallow east dipping fault plane source for the 1755 Lisbon earthquake provided by seismic data,
 1041 gravity and thermal modeling. *Tectonophysics*, 426(1-2), 135-152.
- 1042 Thingbaijam, K. K. S., Martin Mai, P., Goda, K. (2017). New empirical earthquake source- scaling laws.
 1043 *Bulletin of the Seismological Society of America*, 107(5), 2225–2246. doi: 10.1785/0120170017
- 1044 Vermeesch, P. (2012). On the visualisation of detrital age distributions. *Chemical Geology*, 312- 313,
 1045 190–194. doi: 10.1016/j.chemgeo.2012.04.021
- 1046 Vernant, P., Fadil, A., Mourabit, T., Ouazar, D., Koulali, A., Davila, J. M., Garate, J., McClusky, S.,
 1047 Reilinger, R. (2010). Geodetic constraints on active tectonics of the Western Mediterranean:
 1048 Implications for the kinematics and dynamics of the Nubia-Eurasia plate boundary zone. *Journal of
 1049 Geodynamics*, 49(3-4), 123–129. doi: 10.1016/j.jog.2009.10.007.
- 1050 Vogt, J. (1984). Mouvements de terrain associés aux séismes en Afrique du Nord. *Méditerranée*, 51(1),
 1051 43–48.
- 1052 Wells, D. L., Coppersmith, K. J. (1994). New empirical relationships among magnitude, rupture length,
 1053 rupture width, rupture area, and surface displacement. *Bulletin of the seismological Society of
 1054 America*, 84(4), 974-1002.

- 1055 Zizi, M. (1996). Triassic-Jurassic extension and Alpine inversion in northern Morocco. Mémoires du
1056 Muséum national d'histoire naturelle, 170, 87-101.

ACCEPTED